On generation of lumped mass matrices in partition of unity based methods

Hong Zheng[1, *], Yongtao Yang [2]

[1] Key Laboratory of Urban Security and Disaster Engineering (Beijing University of

Technology), Ministry of Education, Beijing 100124, China

[2] State Key Laboratory of Geomechanics and Geotechnical Engineering, Institute of Rock

and Soil Mechanics, Chinese Academy of Sciences, Wuhan, China

SUMMARY

The partition of unity based methods, such as the extended finite element method (XFEM) or the numerical manifold method (NMM), are able to construct global functions that accurately reflex local behaviors through introducing locally defined basis functions beyond polynomials. In the dynamic analysis of cracked bodies using an explicit time integration algorithm, as a result, huge difficulties arise in deriving lumped mass matrices due to the presence of those physically meaningless degrees of freedom associated with those locally defined functions. Observing no spatial derivatives of trial or test functions exist in the virtual work of inertia force, we approximate the virtual work of inertia force in a coarser manner than the virtual work of stresses, where we inversely utilize the "from local to global" skill. The proposed lumped mass matrix is strictly diagonal and can yield the results in agreement with the consistent mass matrix, but has more excellent dynamic property than the latter. Meanwhile, the critical time step of NMM equipped with an explicit time integration scheme and the proposed mass lumping scheme does not decrease even if the crack in study approaches the mesh nodes – a very excellent dynamic property.

Correspondence to: Hong Zheng, State Key Laboratory of Geomechanics and Geotechnical Engineering, Institute of Rock and Soil Mechanics, Chinese Academy of Sciences, Wuhan 430071, China.
*E-mail: hzheng@whrsm.ac.cn

KEY WORDS: lumped mass matrices; explicit time integration; dynamic crack problems;

critical time step; numerical manifold method

1. INTRODUCTION

The modeling of complex structures in dynamic application is still full of challenges and difficulties. In order to simulate accurately the physical phenomenon involved in dynamic applications such as crash, impact, earthquake and explosion, a very small time step is needed [1]. If implicit time integration algorithms are used, the computational consumption for these simulations with large meshes of complex non-linear structures can become problematic. Therefore, the explicit time integration algorithms becomes popular in dynamic analyses as numerical iterations are not needed at each time step, and also good properties might be obtained in term of accuracy and robustness with possible nonlinearities [2]. Although the explicit time integration algorithm is conditionally stable which requires rather small time steps compared to implicit time integration algorithms, if a lumped mass matrix is adopted instead of the consistent mass matrix, the computational consumption can be reduced significantly as inversing matrices can be avoided in solving the large-scale simultaneous algebraic equations. Therefore, in the dynamic analysis, a lumped mass matrix with excellent numerical properties is always preferable.

The extended finite element method (XFEM) [4, 5], which is considered as an improvement of FEM, was developed to mitigate the burden of meshing and remeshing in modeling crack problems using FEM [3]. XFEM is based on the partition of unity method (PUM) [6], where the representation of a strong or weak discontinuity is achieved via enrichment of the shape functions [7]. The concept of discontinuity enrichment was also used in the element free Galerkin (EFG) method [8-10] which has been successfully used to solve static and dynamic problems [11-13]. So far, XFEM has been successfully used to solve many complex problems such as holes and inclusions [14], two- and three- dimensional static

crack propagation problems [4, 5, 15-17] and dynamic crack propagation problems [18].

As stated previously, mass lumping in dynamic analysis can avoid solving the large-scale simultaneous algebraic equations. However, as discussed in [7], if XFEM is applied to simulate dynamic crack propagation problems, those degrees of freedom associated with enriched shape functions will cause some irregularities in the mass matrix.

Belytschko et al. [18] were the first to point out the critical time step can be very small for XFEM if very small fractions of elements are traversed by a crack. They even pointed out that the critical time step tends to zero as the crack approaches the element nodes, and therefore adopted the implicit-explicit time integration scheme proposed by Hughes and Liu [19]. de Borst et al. [20] also experienced the critical time step problem with discontinuous enrichment. In order to avoid such a situation, they proposed to prevent the crack from crossing an element within a preset distance to a node of the element, compromising the exact orientation of a new crack segment. In addition, Rabczuk et al. [21] proposed to split the particles on both sides of a crack to reflect the displacement skip, which accordingly avoids the introduction of enrichment functions reflecting displacement skip across the crack.

Menouillard et al. [22, 23] have successfully addressed this problem by proposing appropriate mass lumping strategies for enrichment that produce non-zero critical time steps for dynamic crack propagation problems. However, the mass lumping strategies proposed by them are only suitable for discontinuous enrichment. Without the singularity tip enrichment, the crack tip is usually located on the element boundary and accurately locating the crack tip would be very difficult. To resolve this issue, Elguedj et al. [1] further developed a mass lumping scheme for dynamic crack problems with crack-tip enrichment by assuming that all the enriched nodes in an element have equal enriched masses. In their scheme, the kinetic energy of the rigid body modes and the enrichment modes can be preserved. The application of Elguedj's scheme in explicit enriched meshfree method can be found in [7]. Furthermore,

based on a transparent variational approach, a consistent mathematical technique for computing the lumped mass matrix for the partition of unity method is proposed by Schweitzer [24], and applied by Piedade Neto and Baroncini Proenca [25] to solve linear and nonlinear structural dynamic problems in the framework of generalized finite element (GFEM). Schweitzer's approach is applicable to any PUM which adopts a nonnegative partition of unity (PU). In Schweitzer's approach, the consistent mass matrix is converted into a symmetric positive definite block-diagonal matrix rather than a strict diagonal matrix. As a result, solving a system of simultaneous equations with such a block-diagonal matrix as the coefficient matrix will need at least $O(n^3)$ operations.

In 1991, Shi [26] invented the numerical manifold method (NMM), which also falls into the category of the partition of unity. One of the salient advantages of NMM, in our viewpoint, is its ability to solve continuous and discontinuous problems in a unified way because it combines continuum-based FEM and discontinuum-based DDA, an abbreviated word for Discontinuous Deformation Analysis (DDA) [27, 28]. In order to achieve this goal, NMM adopts two cover systems, namely, the mathematical cover and the physical cover. The mathematical cover is utilized to define the partition of unity functions. The physical cover, generated by cutting the mathematical cover with the problem domain, is used to define the local approximations and to integrate the weak form of the problem. In this way, NMM can solve crack propagation problems in a natural way without recourse to any other enrichment functions such as the Heaviside function. Up to now, NMM has been successfully used to model various problems, including static crack problems [29-33], dynamic crack problems [34], Kirchhoff's thin plate bending problems [35], and seepage problems [36-38].

In the original NMM [26], the implicit time integration schemes are used to solve the dynamic problems, where the consistent mass matrix is used. To improve computational efficiency, a mass lumping scheme is proposed in this study. The lumped mass matrix by this

procedure can be combined with the explicit time integration algorithm [39] and applied to dynamic problems in [40].

In this study, a procedure for mass lumping is proposed in the context of NMM, which can produce a strict diagonal matrix. Nevertheless, the procedure is suitable to any partition of unity based method. The critical time steps corresponding to the consistent mass matrices and the proposed lumped mass matrices are compared, indicating that the critical time steps corresponding to the proposed lumped mass matrices are much larger than that to the consistent mass matrix, a very excellent property that XFEM does not have. Accuracy of the proposed mass lumping scheme is investigated by means of solving stationary dynamic crack problems, suggesting the proposed lumped mass matrix can yield results quite agreeable with the consistent mass matrix even if an implicit time integration scheme is adopted.

2. NMM FOR ELASTODYNAMIC PROBLEMS

In this section, the problem definition is formulated, followed by a brief description of NMM. Although the mass lumping scheme to be expounded is implemented in the context of NMM, it is suitable for any partition of unity based methods.

2.1 Governing equations in strong form

Considering a 2D homogeneous, isotropic and linear elastic problem defined on domain Ω with the boundary $\partial\Omega = \Gamma = \Gamma_u \cup \Gamma_t \cup \Gamma_c$, as shown in Fig. 1. Here, Γ_u is the displacement boundary; Γ_t the traction boundary; and Γ_c the crack surface, defined by $\Gamma_c = \Gamma_{c^+} \cup \Gamma_{c^-}$; with Γ_{c^+} and Γ_{c^-} the upper and lower crack surfaces respectively. In terms of displacements as primal variables, the governing equations and the boundary conditions for this problem are as follows:

(1) the equations of momentum conservation

$$\partial^{\mathrm{T}}\boldsymbol{\sigma} + \boldsymbol{b} = \rho \frac{\partial^2 \boldsymbol{u}}{\partial t^2}, \text{ in } \Omega \tag{1}$$

where $\boldsymbol{\sigma}$ is the Cauchy stress vector, $\boldsymbol{b}$ the body force per unit volume, $\boldsymbol{u}$ the displacement vector, ρ the mass density and t the time; ∂ is the matrix of differential operators

$$\partial^{\mathrm{T}} = \begin{bmatrix} \dfrac{\partial}{\partial x} & 0 & \dfrac{\partial}{\partial y} \\[2mm] 0 & \dfrac{\partial}{\partial y} & \dfrac{\partial}{\partial x} \end{bmatrix},\tag{2}$$

(2) the constitutive equation

$$\boldsymbol{\sigma} = \boldsymbol{D}\boldsymbol{\varepsilon}, \text{ in } \Omega \tag{3}$$

where $\boldsymbol{D}$ is the elasticity matrix, and $\boldsymbol{\varepsilon}$ the strain vector related to the displacement vector by

$$\boldsymbol{\varepsilon} = \partial\boldsymbol{u}, \text{ in } \Omega \tag{4}$$

(3) the boundary conditions

$$\boldsymbol{u}(\boldsymbol{x}, t) = \overline{\boldsymbol{u}}(\boldsymbol{x}, t), \text{ on } \Gamma_u \tag{5.1}$$

$$\boldsymbol{\sigma} \cdot \boldsymbol{n} = 0, \text{ on } \Gamma_c \tag{5.2}$$

$$\boldsymbol{\sigma} \cdot \boldsymbol{n} = \overline{\boldsymbol{t}}(\boldsymbol{x}, t), \text{ on } \Gamma_t \tag{5.3}$$

where $\boldsymbol{n}$ is the unit outward normal vector to Γ_t, $\overline{\boldsymbol{t}}$ and $\overline{\boldsymbol{u}}$ are the prescribed traction vector on Γ_t and displacement vector on Γ_u, respectively.

(4) and the initial conditions

$$\boldsymbol{u}(\boldsymbol{x}, 0) = \widetilde{\boldsymbol{u}}(\boldsymbol{x}), \text{ in } \Omega \tag{6.1}$$

$$\dot{\boldsymbol{u}}(\boldsymbol{x}, 0) = \dot{\widetilde{\boldsymbol{u}}}(\boldsymbol{x}), \text{ in } \Omega \tag{6.2}$$

where $\widetilde{\boldsymbol{u}}(\boldsymbol{x})$ and $\dot{\widetilde{\boldsymbol{u}}}(\boldsymbol{x})$ are the initial displacement and velocity fields, respectively.

2.2 Fundamentals of NMM

In this section, the basic concepts of the numerical manifold method (NMM) are briefly introduced, more details about NMM can be found in [41]. NMM involves three important concepts, i.e., the mathematical cover, the physical cover and the manifold elements.

The mathematical cover consists of a set of user-defined overlapping patches, Ω_i^m, $i = 1, \cdots, n^m$. Each patch, Ω_i^m, is a simply connected domain named as mathematical patch,

and n^m the number of mathematical patches. The mathematical cover is independent of, but must cover the whole problem domain Ω.

The physical cover consists of all the physical patches, and the physical patches are obtained by cutting the mathematical patches with the components of the problem domain. Here, the components of the problem domain include the domain boundaries, the material interfaces and the discontinuities. When a mathematical patch Ω_i^m is divided into several disjointed domains, only those inside the problem domain form the physical patches and those outside the problem domain are discarded. A mathematical patch Ω_i^m might be divided into more than one physical patch Ω_{j-i}^p, $j = 1, \cdots, n_i^p$. Here Ω_{j-i}^p is called the j-th physical patch generated from the ith mathematical patch Ω_i^m. n_i^p is the number of all the physical patches that are generated from the same mathematical patch Ω_i^m. As a result, the cutting operations make the physical patches exactly cover and match the problem domain Ω.

Further, a manifold element is defined as the common region of several physical patches. All the manifold elements constitute a mesh of the problem domain and match the problem domain exactly. The manifold elements are the basic units for integrating the weak form of the problem.

To explain the above mentioned concepts, the example present in Fig. 2 is used. The regular triangular mesh is used to form the mathematical cover, and the thick red lines define problem domain Ω. The regular mesh used here is called the mathematical mesh. The mathematical mesh does not have to match the boundary or crack, but must cover the problem domain Ω. A circular red dot represents the center of the corresponding mathematical patch, which is a hexagon marked by yellow edges. Cutting mathematical patch Ω_7^m with Γ yields two physical patches, namely, Ω_{1-7}^p and Ω_{2-7}^p. Cutting Ω_9^m with Γ, only the fraction inside Ω forms the physical patch, namely, Ω_{1-9}^p, and the rest part of Ω_9^m is discarded. Since all Ω_4^m is totally inside the problem domain, Ω_4^m is not cut off at all, and

only one physical patch Ω_{1-4}^{p} is generated, which coincides with Ω_{4}^{m}. All the physical patches generated from the mathematical patches constitute the physical cover, or the physical mesh in this particular case.

It should be pointed out that each physical patch, say Ω_{1-7}^{p}, corresponds to one and only one NMM node, denoted by N_{1-7}^{p}. Similar to FEM, the degrees of freedom over a physical patch are attached at the NMM node of the physical patch. But an NMM node has two types, namely, a real node and a phantom node. A real node is within the domain of the physical patch, such as N_{1-7}^{p}, while a phantom node is outside the domain of the physical patch, such as N_{2-7}^{p}. The concept of phantom nodes can also be found in [42].

Under the small deformation and small rotation assumption, all the physical patches generated from the same mathematical patch have their own NMM nodes that are all at the center of the mathematical patch. As can be seen in Fig. 3(a), both N_{1-7}^{p} and N_{2-7}^{p} coincide with the center of Ω_{7}^{m}. If large movement is involved, however, all the NMM nodes will move with their physical patches. As a result, only at the outset do N_{1-7}^{p} and N_{2-7}^{p} coincide; later on, they might separate because the crack runs through the problem domain (Fig. 3(b)). More details can be found in [43]. In the rest of this study, the ''NMM node'' will also be termed as ''node'' for simplicity in presentation. Meanwhile, once the physical cover is formed, the mathematical cover will not be employed in the next time step. Subsequently, patches are actually referring to physical patches.

In this study, two types of patches, e.g. nonsingular patches and singular patches are considered. The nonsingular patches do not contain any crack tips, like Ω_{1-4}^{p} and Ω_{1-9}^{p}, while the singular patches contain at least one crack tip, like Ω_{1-8}^{p}, as shown in Fig. 2.

The common region of neighboring physical patches will produce a manifold element. For example, Ω_{1-4}^{p}, Ω_{1-5}^{p} and Ω_{1-6}^{p} produce the manifold element,

$$E_2 = \Omega_{1-4}^p \cap \Omega_{1-5}^p \cap \Omega_{1-6}^p,$$

which is a perfect equilateral triangle, while Ω_{1-1}^p, Ω_{1-2}^p and Ω_{1-3}^p produce the manifold element,

$$E_1 = \Omega_{1-1}^p \cap \Omega_{1-2}^p \cap \Omega_{1-3}^p,$$

which is an incomplete triangle. E_1 and E_2 are the green area shown in Fig. 2.

Over each mathematical patch (Ω_i^m), a weight function $w_i(\boldsymbol{x})$, will be defined, which satisfies

$$w_i(\boldsymbol{x}) = 0, \text{ if } \boldsymbol{x} \notin \Omega_i^m; \tag{7.1}$$

$$0 \leq w_i(\boldsymbol{x}) \leq 1, \text{ if } \boldsymbol{x} \in \Omega_i^m; \tag{7.2}$$

$$\sum_i w_i(\boldsymbol{x}) = 1, \text{ if } \boldsymbol{x} \in \Omega. \tag{7.3}$$

The weight function, $w_i(\boldsymbol{x})$ associated with Ω_i^m will be accordingly transferred to physical patches, Ω_{j-i}^p, $j = 1, \cdots, n_i^p$, and denoted as $w_{j-i}(\boldsymbol{x})$, $j = 1, \cdots, n_i^p$. $w_{j-i}(\boldsymbol{x})$, $j = 1, \cdots, n_i^p$, may have the same expression as $w_i(\boldsymbol{x})$, but they have totally different domains of definition. Besides, over each Ω_{j-i}^p, different local approximation functions will be defined. This enables NMM to simulate discontinuity across a crack without recourse to the Heaviside function.

For convenience, all the physical patches Ω_{j-i}^p and weight functions $w_{j-i}(\boldsymbol{x})$ are coded with a single subscript and denoted as Ω_k^p and $w_k(\boldsymbol{x})$, respectively. Here, n^p is the number of all the physical patches or the nodes, equal to

$$n^p = \sum_i n_i^p . \tag{8}$$

Over each Ω_j^p, the local displacement vector $\boldsymbol{u}_j^h(\boldsymbol{x})$ can be defined, which reflects the asymptotic behavior of solution over the patch. Thanks to the partition of unity of the weight functions $\{w_j(\boldsymbol{x})\}$, the local approximation $\boldsymbol{u}_j^h(\boldsymbol{x})$ over Ω_j^p can take any expressions but no

variational crime is committed [43]. To avoid unnecessary distractions, nevertheless, this study takes a constant vector as the local displacement vector over nonsingular patch Ω_j^p, resulting in

$$\boldsymbol{u}_j^h(\boldsymbol{x}) = \boldsymbol{u}_j. \tag{9}$$

Such a selection avoids linear dependence problem [41]. Here, $\boldsymbol{u}_j$ represents the translational displacement vector of NMM node N_j^p.

If, however, patch Ω_j^p contains a crack tip, we can enrich the displacement approximation over Ω_j^p by adding some particular functions that reflect the local behavior of solution around the crack tip, such as,

$$\boldsymbol{u}_j^h(\boldsymbol{x}) = \boldsymbol{u}_j + \boldsymbol{f}_j(r,\theta), \tag{10}$$

with

$$\boldsymbol{f}_j(r,\theta) = \boldsymbol{E}_j(r,\theta)\boldsymbol{e}_j, \tag{11}$$

$\boldsymbol{e}_j$ is the 8-dimensioanl vector consisting of eight enrichment degrees of freedom

$$\boldsymbol{e}_j^{\mathrm{T}} = \left(e_j^1, \cdots, e_j^8\right), \tag{12}$$

$\boldsymbol{E}_j(r,\theta)$ is the 2×8 matrix with four enrichment functions or local basis functions

$$\boldsymbol{E}_j = [c_1\boldsymbol{I}_2 \ \ s_1\boldsymbol{I}_2 \ \ c_2\boldsymbol{I}_2 \ \ s_2\boldsymbol{I}_2], \tag{13}$$

where $\boldsymbol{I}_2$ is the 2×2 identity matrix, (c_1, s_1) and (c_2, s_2) are from the first two items of Williams' displacement series, defined by

$$c_k(r,\theta) = \sqrt{r}\cos\frac{2k-1}{2}\theta, \ \ s_k(r,\theta) = \sqrt{r}\sin\frac{2k-1}{2}\theta, \tag{14}$$

with $k = 1$ and 2. Here, (r,θ) is the polar coordinate with the origin at the crack tip, the crack extension line as the polar axis, and $-\pi < \theta \leq \pi$.

Equations (9) and (10) can be written in the unified form

$$\boldsymbol{u}_j^h(\boldsymbol{x}) = \boldsymbol{L}_j(\boldsymbol{x})\boldsymbol{d}_j, \ \ \forall \boldsymbol{x} \in \Omega_j^p, \tag{15}$$

with the vector

$$d_j = u_j, \text{ for nonsingular } \Omega_j^p, \tag{16.1}$$

or

$$d_j = \begin{pmatrix} u_j \\ e_j \end{pmatrix}, \text{ for singular } \Omega_j^p, \tag{16.2}$$

and the matrix

$$L_j = I_2, \text{ for nonsingular } \Omega_j^p, \tag{16.3}$$

or

$$L_j = [I_2, E_j], \text{ for singular } \Omega_j^p, \tag{16.4}$$

which is discontinuous across the crack.

As a result, associated with a physical patch Ω_j^p is the triple $\left(\Omega_j^p; u_j^h; w_j\right)$, reflecting the local region, the local approximation and the proportion of the local approximation to the global approximation, respectively.

By adding up the weighted approximations, $w_j u_j^h$, over all the n^p physical patches, we obtain the global approximation to the displacement vector over Ω

$$u^h(x) = \sum_j w_j(x) u_j^h(x), \ \forall x \in \Omega. \tag{17}$$

To this point, it is clear that the two major differences exist between FEM and NMM. First, if a finite element mesh is rendered to match the problem domain Ω, namely let the mathematical mesh coincide with the physical mesh, and let all the local functions over the relevant patches be taken as unknown constants, then NMM reduces to FEM. And second, even if the mathematical mesh coincides exactly with the physical mesh, functions $\{w_i\}$ in FEM are regarded as the shape functions and accordingly compose the so called FEM space with $\{w_i\}$ as the basis, in which a function, actually an approximation to the solution, can only be expressed as a linear combination of these basis functions $\{w_i\}$. While the same functions $\{w_i\}$ are viewed in NMM as the weight functions; and an NMM approximation is

expressed as the sum of all the local functions multiplied by the weight functions over the corresponding patches. All functions created in this way constitute the NMM space, a proper subspace of the space of admissible functions of solution such as $H^1(\Omega)$ for second order problems.

Of course, covers of other types are allowed in NMM, such as the cover consisting of the supports of shape functions in the moving least squares technique, see [32, 38, 43] for example.

Substituting equation (15) into equation (17) results in

$$u^h(x) = N(x)d, \ \forall x \in \Omega. \tag{18}$$

Here, d is the vector consisting of degrees of freedom of all the physical patches, and $N(x)$ is the shape matrix defined by

$$N(x) = [N_1, \cdots, N_{n^p}]. \tag{19}$$

$N(x)$ is discontinuous across any discontinuity, weak or strong; $N_j(x)$ is the shape function matrix of the jth physical patch

$$N_j(x) = w_j(x)L_j(x), \tag{20}$$

which vanishes outside Ω_j^p.

It is mentioned that although the weight functions $\{w_j(x)\}$ satisfy the partition of unity (PU) property, in general $\{N_j(x)\}$ do not have the PU property in those regions near the crack tips due to the introduction of the enrichment functions.

In addition, we mention that if an equally distributed error field is sought, the adaptive analysis can be conducted. In this situation, multilayer covers can be deployed to wherever high gradient of stress exists, which has been thoroughly expounded in [31].

2.3 Weak-form and discrete version

The discrete equations of NMM for the initial-boundary value problem of equations (1-6) are generated from the weak form and expressed as

$$\int_\Omega \rho \delta \boldsymbol{u}^{\mathrm{T}} \ddot{\boldsymbol{u}} + \int_\Omega (\delta \boldsymbol{\varepsilon})^{\mathrm{T}} \boldsymbol{D} \boldsymbol{\varepsilon} = \int_\Omega \delta \boldsymbol{u}^{\mathrm{T}} \boldsymbol{b} + \int_{\Gamma_t} \delta \boldsymbol{u}^{\mathrm{T}} \bar{\boldsymbol{t}} , \qquad (21)$$

where $\boldsymbol{\varepsilon}$ is related to $\boldsymbol{u}$ by equation (4), and $\delta \boldsymbol{u}$ is virtual displacement vector. Equation (21) is equivalent to equations (1), (5.2) and (5.3). Here, the first item is the virtual work of inertia force and will be approximated in the next section. The second item is known as the virtual work of stress.

Throughout this study, the convention of integral notation in differential topology, see [44] for example, is followed, where the differential elements, such as the differential area $d\Omega$ and the differential arc-length dS in equation (21), are totally omitted. There are two major reasons for this: firstly from the subscripts of the integral sign we immediately recognize whether the integration is over a domain or a curve; and secondly length of the equation can be shorten. On the basis of the analysis on manifolds, in addition, NMM should follow the conventions of the subject as far as possible.

By direct substituting the displacement function of equation (18) into equation (21), a system of the algebraic equations can be obtained as follows:

$$\boldsymbol{M} \ddot{\boldsymbol{d}} + \boldsymbol{K} \boldsymbol{d} = \boldsymbol{f}, \qquad (22)$$

where $\boldsymbol{d}$ is the vector consisting of degrees of freedom of all the physical patches, $\ddot{\boldsymbol{d}}$ is the second time derivative of $\boldsymbol{d}$ or the acceleration vector. $\boldsymbol{M}$, $\boldsymbol{f}$ and $\boldsymbol{K}$ are the global mass matrix, global nodal force vector and global stiffness matrix, respectively, and defined as

$$\boldsymbol{M} = \int_\Omega \rho \boldsymbol{N}^{\mathrm{T}} \boldsymbol{N} , \qquad (23)$$

$$\boldsymbol{K} = \int_\Omega \boldsymbol{B}^{\mathrm{T}} \boldsymbol{D} \boldsymbol{B} , \qquad (24)$$

$$f = \int_\Omega N^T b + \int_{\Gamma_t} N^T \bar{t}, \tag{25}$$

with $B = \partial N$, and the definition of operator ∂ is defined in equation (2). The mass matrix M given in equation (23) is known as the consistent mass matrix, with the same sparsity structure as K. By "consistent", it is meant that the approximation to the integrand of the virtual work of inertia force is conducted in the same way as the approximation to the virtual work of internal force.

Due to the introduction of enrichment degrees of freedom, the component functions of matrix N in equation (23) do not have in general the PU property in those regions near the crack tips; as a result, the mass matrix M in equation (23) cannot be expected to satisfy the mass conservations, because Liu [45] have proved that the PU property is necessary and sufficient for the mass conservation, which says that the summation of all the elements of M corresponding to x- or y-direction, keeps conservative.

As an aside, in order to minimize the dispersion error in the finite element analysis of acoustic problems, He et al proposed a mass-redistributed FEM [46, 47], where new quadrature points are selected to replace the Gauss points in the numerical integration of the mass matrix M in equation (23). This technique is prospectively applied to the finite element analysis for elasticity.

2.4 The time integration algorithm

Suppose that the state at the time step n is known; in other words, the degrees of freedom vector d_n, its speed $\dot{d}_n$, and accelerator $\ddot{d}_n$ are all given. By using the Newmark time integration, the vector d and its speed vector $\dot{d}$ at the $(n + 1)$ time step, denoted by d_{n+1} and $\dot{d}_{n+1}$ respectively, can be calculated

$$d_{n+1} = d_n + \Delta t \dot{d}_n + \frac{\Delta t^2}{2}\left[(1 - \beta_2)\ddot{d}_n + \beta_2 \ddot{d}_{n+1}\right], \tag{26}$$

$$\dot{d}_{n+1} = \dot{d}_n + \Delta t\left[(1 - \beta_1)\ddot{d}_n + \beta_1 \ddot{d}_{n+1}\right], \tag{27}$$

in terms of vector $\ddot{\boldsymbol{d}}_{n+1}$.

Solving system (22) at the time step $n + 1$ for $\ddot{\boldsymbol{d}}_{n+1}$ and using equation (26), we have

$$\bar{\boldsymbol{M}}\ddot{\boldsymbol{d}}_{n+1} = \bar{\boldsymbol{f}}, \tag{28}$$

with

$$\bar{\boldsymbol{M}} = \boldsymbol{M} + \frac{1}{2}\beta_2 \Delta t^2 \boldsymbol{K}, \tag{28.1}$$

and

$$\bar{\boldsymbol{f}} = \boldsymbol{f}_{n+1} - \boldsymbol{K}\left[\boldsymbol{d}_n + \Delta t \dot{\boldsymbol{d}}_n + \frac{1}{2}(1 - \beta_2)\Delta t^2 \ddot{\boldsymbol{d}}_n\right]. \tag{28.2}$$

Here, both β_1 and β_2 are user-specified parameters, falling in the integral [0, 1]. The scheme corresponding to $\beta_2 \geq \frac{1}{2}$ gives rise to unconditionally stable implicit schemes, at the cost of the inverse of $\bar{\boldsymbol{M}}$ in solving system (28).

The practice corresponding to $\beta_2 = 0$ is known as the explicit time integration scheme. But this is a conditionally stable process in which the time step length Δt must be small enough. If, however, the mass matrix $\boldsymbol{M}$ is diagonal, solving system (28) becomes a very easy task, and the dynamic process can be thus speeded up significantly.

2.5 Interaction integral and dynamic stress intensity factors

In the dynamic crack analysis, the dynamic stress intensity factor (DSIF) characterizes the singularity strength of the stress distribution around the crack tip, and plays a very important role in the failure analysis [48]. To obtain the DSIFs, the domain form of interaction integrals is employed in this study. Two states of the cracked body are considered. State $1\left(\sigma_{ij}^{(\text{real})}, \varepsilon_{ij}^{(\text{real})}, u_i^{(\text{real})}\right)$ corresponds to the actual state while state $2\left(\sigma_{ij}^{(\text{aux})}, \varepsilon_{ij}^{(\text{aux})}, u_i^{(\text{aux})}\right)$ is an auxiliary state which is chosen as the asymptotic fields for modes I and II. The Interaction integral with the mixed-mode DSIFs can be obtained by [49]

$$I^{(\text{real,aux})} = -\int_{A_J} \left(W^{(\text{real,aux})} \delta_{1j} - \sigma_{ij}^{(\text{real})} \frac{\partial u_i^{(\text{aux})}}{\partial x_1} \right) \frac{\partial q}{\partial x_j} dA +$$

$$\int_{A_J} \left[\sigma_{ij}^{(\text{aux})} \frac{\partial u_i^{(\text{real})}}{\partial x_1} \frac{\partial q}{\partial x_j} + \rho \left(\frac{\partial^2 u_j^{(\text{real})}}{\partial t^2} \frac{\partial u_j^{(\text{aux})}}{\partial x_1} \right) q \right] dA \qquad (29)$$

in which $W^{(\text{real,aux})}$ is the interaction strain energy defined as

$$W^{(\text{real,aux})} = \sigma_{ij}^{(\text{real})} \varepsilon_{ij}^{(\text{aux})} = \sigma_{ij}^{(\text{aux})} \varepsilon_{ij}^{(\text{real})} \qquad (30)$$

A_J is the area-path determined by a circle with radius R shown in Fig. 4. R is called interaction integral domain radius and defined as

$$R = R_d h, \qquad (31)$$

in which h is the maximum circumradius of a mathematical patch, R_d is a factor which can determine the size of the circle. $q(x)$ is a bounded weighting function, which is schematically represented in Fig. 4, the value of which is 1 within the circle and 0 outside the circle.

Alternatively, for a general mixed-mode crack the relationship between the J-integral and the dynamic stress intensity factors is given by

$$I^{(\text{real,aux})} = \frac{2}{E'} \left(K_{\text{I}}^{\text{dyn}} K_{\text{I}}^{\text{aux}} + K_{\text{II}}^{\text{dyn}} K_{\text{II}}^{\text{aux}} \right), \qquad (32)$$

in which

$$E' = \begin{cases} E & \text{plane stress} \\ \dfrac{E}{1 - v^2} & \text{plane strain} \end{cases}.$$

$K_{\text{I}}^{\text{aux}}$ and $K_{\text{II}}^{\text{aux}}$ are the DSIFs corresponding to the auxiliary state. The DSIFs for the current state can be determined by selecting the State 2 appropriately [49].

3. MASS LUMPING AND CRITICAL TIME STEPS

In this section, we first present the scheme of mass lumping. Then, we will demonstrate the lumped mass matrix proposed by the lumping scheme has a more excellent dynamic property than the consistent mass matrix because the former has a larger critical time step for the same mesh.

3.1 Mass lumping

As stated previously, only if the mass matrix $\boldsymbol{M}$ is diagonal, the explicit time scheme becomes meaningful. In this section, the mass lumping scheme is proposed in the framework of NMM. To this end, let's write separately out the virtual work of the inertia force as follows

$$\delta W_I = \int_\Omega \rho (\delta \boldsymbol{u})^{\mathrm{T}} \ddot{\boldsymbol{u}}. \tag{33}$$

Due to the partition of unity of the weight functions $\{w_i\}$, $\sum w_i$ can be multiplied with the integrand of δW_I, leading to

$$\delta W_I = \int_\Omega \rho (\delta \boldsymbol{u})^T \ddot{\boldsymbol{u}} \sum_i w_i = \sum_i \int_\Omega \rho w_i (\delta \boldsymbol{u})^{\mathrm{T}} \ddot{\boldsymbol{u}}. \tag{33.1}$$

Compactness of the support of each $w_i(\boldsymbol{x})$, namely, $w_i(\boldsymbol{x}) = 0$ for $\boldsymbol{x} \notin \Omega_i^p$, reduces δW_I to

$$\delta W_I = \sum_i \int_{\Omega_i^p} \rho w_i (\delta \boldsymbol{u})^{\mathrm{T}} \ddot{\boldsymbol{u}}. \tag{33.2}$$

The above procedure actually comes from the definition of integral of a scalar function over a compact manifold [44]. Here, the manifold reduces to the problem domain Ω in the 2-dimentional Euclidean space, and the scalar function is the integrand $\rho w_i (\delta \boldsymbol{u})^{\mathrm{T}} \ddot{\boldsymbol{u}}$.

From the perspective of calculus of variations, the calculation of δW_I does not have to demand $\delta \boldsymbol{u}$ or $\ddot{\boldsymbol{u}}$ belonging to $H^1(\Omega)$ like the calculation of $\boldsymbol{K}$ in equation (24). Instead, it is enough for $\delta \boldsymbol{u}$ and $\ddot{\boldsymbol{u}}$ in δW_I to belong to $L^2(\Omega)$. Further, if Ω_i^p is small enough,

both $\delta \boldsymbol{u}$ and $\ddot{\boldsymbol{u}}$ in Ω_i^p can be replaced approximately by their local values on Ω_i^p itself, $\delta \boldsymbol{u}_i^h$ and $\ddot{\boldsymbol{u}}_i^h$, respectively, with no variational crime committed. As a result,

$$\delta W_I \approx \sum_i \delta W_I^i, \tag{34}$$

with

$$\delta W_I^i = \int_{\Omega_i^p} \rho w_i (\delta \boldsymbol{u}_i^h)^{\mathrm{T}} \ddot{\boldsymbol{u}}_i^h. \tag{35}$$

Here, we have to admit that we actually utilize inversely the skill of "from local to global" in differential topology.

Using equation (15),

$$\delta \boldsymbol{u}_i^h = \boldsymbol{L}_i \delta \boldsymbol{d}_i, \tag{36}$$

and

$$\ddot{\boldsymbol{u}}_i^h = \boldsymbol{L}_i \ddot{\boldsymbol{d}}_i, \tag{37}$$

and substituting equations (36) and (37) into equation (35), we have the virtual work of Ω_i^p

$$\delta W_I^i = (\delta \boldsymbol{d}_i)^{\mathrm{T}} \boldsymbol{M}_I^i \ddot{\boldsymbol{d}}_i, \tag{38}$$

with $\boldsymbol{M}_I^i$ being the mass matrix of patch Ω_i^p,

$$\boldsymbol{M}_I^i = \int_{\Omega_i^p} \rho w_i \boldsymbol{L}_i^{\mathrm{T}} \boldsymbol{L}_i. \tag{39}$$

which is a positive and definite matrix, and will be termed the first lumping scheme.

If Ω_i^p is an ordinary patch, $\boldsymbol{L}_i = \boldsymbol{I}_2$ according to equation (16.3), then $\boldsymbol{M}_I^i$ is a 2×2 diagonal matrix defined by

$$\boldsymbol{M}_I^i = \bar{\rho} \boldsymbol{I}_2, \tag{40}$$

with

$$\bar{\rho} = \int_{\Omega_i^p} \rho w_i. \tag{40.1}$$

If Ω_i^p is a singular patch, then, $\boldsymbol{L}_i = [\boldsymbol{I}_2, \boldsymbol{E}_i]$ according to equation (16.4).

Since $w_i(\boldsymbol{x}) \geq 0$, $\boldsymbol{x} \in \Omega_i^p$, $\boldsymbol{M}_I^i$ can also be approximated as follows

$$\boldsymbol{M}_I^i = \frac{\overline{\rho}}{S_i^p} \int_{\Omega_i^p} \boldsymbol{L}_i^{\mathrm{T}} \boldsymbol{L}_i . \tag{41}$$

with S_i^p = area of Ω_i^p. Equation (41) is actually derived from further smoothing the integrand (39), and will be called the second lumping scheme in the subsequent. Both the two lumping schemes has little difference.

To this point, the lumped global mass matrix $\boldsymbol{M}$ is derived by integrating patch-by-patch rather than element-by-element as in any other numerical methods. $\boldsymbol{M}$ has only the diagonal block $\boldsymbol{M}_I^i$ corresponding to patch Ω_i^p and all the off-diagonal blocks are nil blocks.

For a singular patch Ω_i^p, however, $\boldsymbol{M}_I^i$ defined in either equation (39) or equation (41) is a 10×10 matrix with off-diagonal items. Fortunately, it is positive and definite, and can be easily diagonalized as

$$\boldsymbol{M}_I^i = \boldsymbol{P}_i \boldsymbol{D}_i \boldsymbol{P}_i^T , \tag{42}$$

according to the spectral decomposition theorem; where $\boldsymbol{D}_i$ is a 10×10 diagonal matrix with all the diagonal items being positive, namely, the eigenvalues of $\boldsymbol{M}_I^i$; and $\boldsymbol{P}_i$ is a 10×10 orthogonal matrix, i.e., $\boldsymbol{P}_i^{-1} = \boldsymbol{P}_i^{\mathrm{T}}$.

If the diagonal block $\boldsymbol{D}_i$ rather than $\boldsymbol{M}_I^i$ are at the diagonal of $\boldsymbol{M}$ for the singular patch-i, then the i-th sub-matrix column $\boldsymbol{K}_{:,i}$ of the global stiffness matrix $\boldsymbol{K}$ is post-multiplied by $\boldsymbol{P}_i$, namely,

$$\boldsymbol{K}_{:,i} \leftarrow \boldsymbol{K}_{:,i} \boldsymbol{P}_i ;$$

followed by pre-multiplication of the i-th sub-matrix row $\boldsymbol{K}_{i,:}$ by $\boldsymbol{P}_i^{\mathrm{T}}$, namely,

$$\boldsymbol{K}_{i,:} \leftarrow \boldsymbol{P}_i^{\mathrm{T}} \boldsymbol{K}_{i,:}$$

Here, "$\leftarrow$" represents "is replaced by". After these operations are carried out, the global

stiffness matrix $\boldsymbol{K}$ still keeps symmetric and positive definite. Correspondingly, the load vector $\boldsymbol{f}$ in equation (25) should be adjusted to its i-th sub-vector $\boldsymbol{f}_i$ by

$$\boldsymbol{f}_i \leftarrow \boldsymbol{P}_i^{\mathrm{T}} \boldsymbol{f}_i.$$

From the solution of the NMM system, as a result, what we will obtain are actually

$$\boldsymbol{d}_i' = \boldsymbol{P}_i^{\mathrm{T}} \boldsymbol{d}_i, \tag{43}$$

attached to the singular patch Ω_i^p. Since $\boldsymbol{P}_i$ is orthogonal, once the NMM system is solved, we can immediately have $\boldsymbol{d}_i$ by

$$\boldsymbol{d}_i = \boldsymbol{P}_i \boldsymbol{d}_i'. \tag{44}$$

Clearly, the above derivation of the lumped mass matrix $\boldsymbol{M}$ does not introduce any assumptions as in [7], where the first lumping strategy is based on the assumption that all the nodes influencing an integration cell have the same proportional quality of the integration cell; and the second lumping strategy is based on the physical intuition that the lumped mass matrix preserves the kinetic energy of the body corresponding to a particular translational movement.

It is mentioned that due to the introduction of enhancement functions the shape functions loss the PU property, concluding that the mass conservation does not hold in either x- or y-direction. However, the mass matrix $\boldsymbol{M}$ proposed in the above procedure still keeps mass conservative for those items representing translational components.

In the conventional finite element analysis where no enhancement function is introduced, the mass conservation is an intuitive "law" that is followed while deriving the lumped mass matrix. It's still an open issue, from our viewpoint, whether the mass conservation should be kept if the enhancement functions are introduced. The goal of this study is to gain a better lumped mass matrix than the consistent one defined in equation (23) in both accuracy and dynamic properties.

3.2 Critical time step analysis

The explicit time integration scheme, as is well known, is conditionally stable, implying the time step Δt should be chosen in accordance with the Courant-Freidrich-Lewy condition [1]

$$\Delta t \leq \Delta t_c = \frac{2}{\omega_{\max}}, \tag{45}$$

where Δt_c is the critical time step, and $\omega_{\max}$ is the maximum eigenfrequency determined by the generalized eigenvalue problem [7]

$$\det\left(\boldsymbol{K} - \omega^2 \boldsymbol{M}\right) = 0. \tag{46}$$

In practice, we refer to an explicit time integration scheme with a greater critical time step Δt_c as better dynamic property.

In the following, for the same stiffness matrix $\boldsymbol{K}$ we will compare the critical time steps corresponding to the proposed lumped mass matrix, denoted by $\boldsymbol{M}_{lump}$, and the consistent mass matrix, represented by $\boldsymbol{M}_{consist}$.

To this end, the 5×5 mesh and the 10×10 mesh are designed with and without cracks, and with different crack tip positions, being considered, as shown in Figs. 5 and 6, respectively.

First, we calculate the critical time steps correspond to $\boldsymbol{M}_{consist}$ and $\boldsymbol{M}_{lump}$ with the two meshes containing no crack (Fig. 5(a) and Fig. 6(a)), and list the results in Table 1. Since no singular patch exists, $\boldsymbol{M}_{lump}$ corresponding to equation (39) is the same as that to equation (41). Two conclusions can be drawn:

(1) For a given problem domain, if it is discretized with a finer mesh, the critical time step will become smaller. This will be used in the following discussion.

(2) And the critical time steps corresponding to $\boldsymbol{M}_{lump}$, Δt_{lump}'s are much larger than those to $\boldsymbol{M}_{consist}$, Δt_{lump}'s. The similar conclusions were also drawn in [50].

Second, let a crack cut through the problem domain, with the crack varying vertically, as

shown in Fig. 5(b) and Fig. 6(b).

Third, let a crack partially cut the problem domain, with the crack varying vertically, as shown in Fig. 5(c) and Fig. 6(c).

Last, let a crack partially cut the problem domain, with the crack tip varying horizontally, as shown in Fig. 5(d) and Fig. 6(d).

The critical time steps corresponding to the above crack deployments are shown in Fig. 7 and Fig. 8. For convenience of observation, the results in Fig. 7 are normalized with Δt_{lump} of mesh 5×5; while the results in Fig. 8 are normalized with Δt_{lump} of mesh 10×10. Since the results of Fig. 7 and Fig. 8 have the similar trend, we only discuss the results presented in Fig. 7. Some conclusions can be drawn from Fig. 7:

(1) For the first crack deployment scheme (Fig. 5(b)), namely, the crack cutting through the problem domain, Δt_{lump1} and Δt_{lump2} are completely identical, which are both much larger than $\Delta t_{consist}$, as shown in Fig. 7(a). The values of Δt_{lump1} and Δt_{lump2} depend on the crack position. Δt_{lump1} (assessed by the first lumping scheme, equation (39)) and Δt_{lump2} (evaluated by the second lumping scheme, equation (41)) reach the maximum when the crack is directly cross the nodes, namely, the relative crack position is equal to zero or one. This is a very good property of NMM of which XFEM is not in possession [18]. Although Δt_{lump1} and Δt_{lump2} have a drop when the crack get away from the nodes, Δt_{lump1} and Δt_{lump2} will increase as the crack gets close to the middle of the mesh.

(2) For the second crack deployment scheme (Fig. 5(c)), namely, the crack partially cutting the problem domain and varying vertically, Δt_{lump2} is a little larger than Δt_{lump1}, and both are much larger than $\Delta t_{consist}$, as shown in Fig. 7(b).

(3) For the third crack deployment scheme (Fig. 5(d)), namely, the crack tip moving horizontally, Δt_{lump2} is generally larger than Δt_{lump1}, and both are much larger than $\Delta t_{consist}$, as shown in Fig. 7(c). Δt_{lump1}, Δt_{lump2} and $\Delta t_{consist}$ are still quite large even

while the crack tip approaches the element boundary.

In all the cases, the critical time step corresponding to $\boldsymbol{M}_{lump}$ is much larger than that to $\boldsymbol{M}_{consist}$, suggesting that the proposed lumped mass matrix has more excellent dynamic property. As for the critical time step corresponding to equation (39) or equation (41), no essential difference exists, but the critical time step corresponding to equation (41), Δt_{lump2} is slightly larger than that to equation (39), Δt_{lump1}. For example, in Fig. 7, $\min(\Delta t_{lump1})=$ 0.19, and $\min(\Delta t_{lump2})$ =0.20.

4. NUMERICAL EXAMPLES

In this section, to investigate accuracy of the proposed mass lumping scheme, two numerical examples of stationary cracks under dynamic load are considered, and the results are compared with the analytical solution.

Meanwhile, as a demonstration of the effect of the proposed mass lumping scheme, the dynamic response of a laminated cantilever is analyzed under the action of a transient load.

4.1 Stationary mode-I semi-infinite crack

An infinite plate with a semi-infinite mode-I crack loaded by a step tensile load (Fig. 9), is considered, with the plane strain condition assumed. The analytical solution for mode-I DSIF is given by Freund [48], which is thus used here for the validation purpose.

We design the finite geometry as in Fig. 10. The parameters are taken as follows: height $2H =$ 4 m, length $L = 10$ m, crack length $a = 5$ m, Young's modulus $E = 210$ GP, Poisson's ratio $v =$ 0.3, density $\rho = 8000$ kg/m^3, step load σ_0 = 500 MPa.

Since the analytical solution for this problem is obtained under the assumption of plate and crack infiniteness, numerical results are only compared with the analytical solution until the tensile stress wave is reflected on the bottom side and reaches again the crack tip [1]. The time needed by the stress wave to reach the crack-tip for the first time is $t_c = H/c_d$ [49], where c_d is the dilatational wave speed. Therefore, the valid time for the simulation is

$t = 3t_c = 3H/c_d = 1.009 \times 10^{-3}$ s. The total computation time for this problem will be set as 0.001s in this study.

The analytical solution of the mode-I DSIF for a stationary crack for this problem is available and can be found in [51]

$$K_{\mathrm{I}}^{\mathrm{dyn}} = \begin{cases} 0, & t < t_c \\ \dfrac{2\sigma_0}{1-v}\sqrt{\dfrac{c_d(t-t_c)(1-2v)}{\pi}}, & t \geq t_c \end{cases} \tag{47}$$

where $c_d = 5944$ m/s.

For the convenience of comparison, the DSIF in this example will be normalized by $K_{\mathrm{I}}^{\mathrm{dyn}}/\sigma_0 H^{0.5}$, while time t by t/t_c.

The discretized models for this problem are shown in Fig. 11.

4.1.1 Validation of the mass lumping scheme

Before the discussion, we validate the proposed lumping scheme using the implicit time integration scheme with constants $\beta_1=\beta_2=1$. Two time steps are set, namely, $\Delta t = 50$ μs and $\Delta t = 100$ μs. The discretized model shown in Fig. 11(c) is used for this test. Shown in Fig. 12 are the results obtained by IMP + Consist, IMP + Lump1 and IMP + Lump2. Here, "IMP" = implicit; Lump1 and Lump2 represents the mass matrix corresponding to equation (39) and equation (41), respectively.

As can be seen in Fig. 12, the results of IMP + Lump1 and IMP + Lump2 are both quite agreeable with IMP + Consist, suggesting the lumped mass matrices proposed by the mass lumping scheme are quite accurate even for quite large time steps.

4.1.2 Influence of interaction integration domain size on accuracy of DSIF

Theoretically, the value of interaction integral should be path independent. However, due to the error in numerical integration, the value of interaction integral is somewhat path dependent. Therefore, the value of R, defined in equation (31), will influence accuracy of the

calculated DSIFs by numerical methods, and an optimum R is of great importance in the crack analysis.

To obtain the optimum value of R, several different R_d (equation (31)) from 0.3 to 1.6 for the computation of the interaction integral as described in Section 2.5 are considered. The discretized model shown in Fig. 11(c) is used for this test and time step Δt is set as 5μs.

In this section, the explicit integration algorithm using the two lumped mass matrices, namely EXP + Lump1 and EXP + Lump2, are conducted. Here, "EXP" = explicit. Shown in Fig. 13 are errors of DSIF corresponding to different interaction integration domain-sizes.

As shown in Fig. 13, the errors of DSIF firstly increase and then decrease over time. When $t = t_c$, the errors reach the maximum value for both EXP + Lump1 and EXP + Lump2 with different R_d. According to the results of Fig. 13, obviously, a value for R_d is recommended in 0.6~1.0. In the following section, R_d will be set as 1.0. It should be noticed that the value of optimum R_d in dynamic crack problems is different from that in static crack problems. Using the implicit time integration scheme in [49], Liu et al. also obtained the optimum value of R_d in dynamic stationary crack problem for singular edge-based smoothed finite element method, and draw similar conclusions to this study.

4.1.3 Convergence of DSIFs versus discretized models

To study the convergence of EXP + Lump1 and EXP + Lump2 in terms of mesh density, three discretized models with 62, 199 and 378 physical patches (PPs) are considered, as shown in Fig. 11. The time step Δt is set as 5μs. The normalized mode-I DSIFs as a function of the normalized time computed by the EXP + Lump1 and EXP + Lump2 are evaluated for each discretized models individually, and the results are then compared with the analytical solution. Fig. 14 presents the convergence of the normalized mode-I DSIFs for the three considered models. As shown in Fig. 14, the normalized values of DSIFs achieved by EXP + Lump1 and EXP + Lump2 converge well to the exact solution as the mesh gets finer.

From Fig. 14, meanwhile it is observed that as the mesh is refined the solution exhibits some oscillations although it, as a whole, approaches to the analytical solution. The phenomenon is caused by the fact that if the explicit time scheme is applied, then the denser the mesh is, the smaller the critical time step becomes, as is pointed out in section 3.2. This suggests that not only the mesh but also the time should be refined simultaneously in order to reach a stably convergent solution. While for the three meshes of different density, one fixed time step, 5μs, is preset, which is very likely to exceed the critical time step associated with the denser mesh. For example, the critical time step of the mesh of 378 patches is about 1.36μs under the condition that the constrained boundary condition is enforced with a penalty of 100E. Besides, the boundary constraint due to the finite model is likely to influence stable convergence of solution. If so, the nonreflecting boundary should be applied to the finite model, which is another big topic.

In addition, the results of EXP + Lump1 and EXP + Lump2 are also drawn in the same figure for all the three discretized models, as shown in Fig. 15, for convenience of comparison. As can be seen in Fig. 15, results of EXP + Lump2 are in agreement with those of EXP + Lump1.

4.1.4 Influence of time step on accuracy of DSIFs

To study the influence of time step on accuracy of EXP + Lump1 and EXP + Lump2, three time steps with $\Delta t = 5, 1$ and 0.2 μs are considered and the discretized model shown in Fig. 11(c) is used. The normalized mode-I DSIFs as a function of the normalized time computed by EXP + Lump1 and EXP + Lump2 are evaluated for each time step individually, and the results are then compared with the theoretical reference solution. Fig. 16 presents the normalized mode-I DSIFs for the three time steps. As shown in Fig. 16, the normalized values of DSIF evaluated by EXP + Lump1 and EXP + Lump2 agree well with the exact solution. As Δt decreases, nevertheless, either EXP + Lump1 or EXP + Lump2 approaches

to the analytical solution in an oscillatory way, and the deep reason for this deserves a further investigation.

In addition, the results of EXP + Lump1 and EXP + Lump2 are also drawn in the same figure for a given time step, as shown in Fig. 17. As can be seen in Fig. 17, again, results of EXP + Lump2 are in agreement with those of EXP + Lump1.

4.2 Edge-crack in a three-point bending beam

As the second example for the stationary dynamic crack problem, a plane strain three-point bending beam is considered. The problem definition is schematically depicted in Fig. 18. Fig. 19 gives the discrete model for this problem. The parameters are taken as depth $W = 0.01$ m, length $L = 0.055$ m, support distance $S = 0.04$ m, crack length $a = 0.005$ m, Young's modulus $E = 210$ GP, Poisson's ratio $v = 0.3$, density $\rho = 7860$ kg/m^3. The beam is subjected to a Heaviside step load as depicted in Fig. 11, and a step load of the amplitude $\sigma_0 = 500$ MPa is applied at the top of the beam over a length of $l = 0.002$ m. The total computation time for this problem will be set as 8.1 μs. The time step Δt is set as 0.001 μs in this section. The mode-I DSIF is evaluated and the computed result is then presented in Fig. 20. For convenience, the computed DSIFs are normalized by the static mode-I SIF [52]

$$K_I^{\text{sta}} = \frac{6Sl\sigma}{4BW^2}\sqrt{\pi a \psi\left(\frac{a}{W}\right)}, \tag{48}$$

$$\psi\left(\frac{a}{W}\right) = 1.09 - 1.735\left(\frac{a}{W}\right) + 8.2\left(\frac{a}{W}\right)^2 - 14.18\left(\frac{a}{W}\right)^3 + 14.57\left(\frac{a}{W}\right)^4. \tag{49}$$

Due to the lack of analytical solution for this problem, a reference solution is calculated by IMP + Consist using the discretized model presented in Fig. 19. The normalized mode-I DSIFs as a function of time evaluated by EXP + Lump1 and EXP + Lump2 are evaluated, and the results are then compared with the reference solution. Fig. 20 presents the normalized

mode-I DSIFs for this problem. As shown in Fig. 20, the normalized values of DSIFs achieved by EXP + Lump1 and EXP + Lump2 agree well with the reference solution.

4.3 Response analysis of a laminated cantilever under a dynamic extension

Shown in Fig. 21 is the tension-time curve acting in the horizontal direction and on the upper beam of the laminated cantilever displayed in Fig. 22. The interface between the two identical beams is smooth and taken as a crack cutting through the corresponding one beam.

Here are the material parameters: Young's modulus $E = 2.0 \times 10^{10}$, Poisson's ratio $v = 0.3$, and the density $\rho = 2650$. The maximum tension $\sigma_0 = 10^6$. The gravity is ignored. The discrete model is displayed in Fig. 23, where 299 patches are generated.

Although it has been successful to avoid using spurious contact springs in DDA [28], there are some technical difficulties to do so in NMM. In this study, therefore, the contact conditions and the essential boundary condition are still enforced using the penalty method, with the contact penalty parameter representing the normal spring stiffness $q_n^c = 10E$, and the essential boundary penalty parameter $q_n^b = 10^7 E$.

The results to be exposed are evaluated by IMP + Lump2 with $\Delta t = 10^{-4} s$, and in excellent agreement with those by IMP + Consist.

Shown in Fig. 24(a) are the horizontal displacement responses of monitored points A and B, see Fig. 22, in the time interval [0, 1] s. Clearly, the horizontal displacement response of the upper point B is much more violent than that of the lower point A, in agreement with our intuition.

In theory, this is a perfectly elastic structure and hence a conservative system. As a result, even after the external load acting at the right end of the upper beam is removed, the upper beam should vibrate periodically forever. However, the behavior illustrated by Fig. 24(a) is not like this. We believe this is because the Newmark time integration algorithm is not symplectic. As we know, in simulating the dynamic behavior of a conservative system, even

those time integration algorithms of high precision, such as the fourth order Runge Kutta method, cannot assure the long-term numerical stability, let along the second order Newmark method. To reflect the long-term behavior, we should employ a symplectic integrator, which will be another important topic and can be referred to Ref [53] for more details.

The details in the time interval [0, 0.1] are displayed in Fig. 24(b). Sure enough, after the external load is removed at $t = 0.04s$, the horizontal displacement of the upper beam behaves approximately periodical during a rather long time period of [0.04, 0.1] − 0.1s = 2.5 times of the loading history. This suggests that the short term results evaluated by the Newmark method are still reliable.

Let's look at the vertical responses of the two beams shown in Fig. 25. After the external load is removed, the Poisson effect corresponding to the horizontal deformation of the upper beam causes it to deform vertically, and further causes the lower beam to deform vertically through the contact between the two beams.

All the observations from the calculated results follows our intuitions. For example, while the upper beam gets longer and thinner under the extension, the lower beam has no deformation because of no contact. Another observation of Fig. 25(a) is that the vertical amplitude of the two beams is in the same order.

5. DISCUSSIONS AND CONCLUSIONS

The mass lumping scheme, which is suitable to any partition of unity based method, is presented in the context of NMM in this study. The lumped mass matrices have the following dynamic properties.

1) critical time steps corresponding to the lumped mass matrices are much larger than those to the consistent mass matrices;

2) for a given problem domain, a finer mesh needs a smaller critical time step;

3) critical time steps generated by the proposed two lumped mass matrices, namely, by

equations (39) and (41), have no essential difference;

4) in contrast to XFEM, the critical time step corresponding to NMM does not decrease even when the crack passes through nodes, namely, it is almost independent upon the crack tip;

5) and even if an implicit time integration scheme is adopted, the results yielded by the proposed lumped mass matrices are in agreement with those by the consistent mass matrices.

In addition, two numerical examples are conducted to evaluate the performance of explicit time integration schemes with the two lumped mass matrices in solving stationary dynamic crack problems. Conclusions are drawn as follows.

1) the optimum value of R_d (equation (31)) for the computation of the interaction integral is 1.0;

2) DSIFs achieved by both EXP + Lump1 and EXP + Lump2 converge well to the exact solution as the mesh gets finer;

3) and results from EXP + Lump1 have no essential difference from EXP + Lump2 and both agree well with analytical solution or reference solution.

Finally, all the analysis results suggest that the lumped matrices are able to supersede the consistent mass matrices in all the situations.

References

1. Elguedj T, Gravouil A, Maigre H. An explicit dynamics extended finite element method. Part 1: mass lumping for arbitrary enrichment functions. Computer Methods in Applied Mechanics and Engineering 2009; 198: 2297-2317.

2. Gravouil A, Elguedj T, Maigre H. An explicit dynamics extended finite element method. Part 2: Element-by-element stable-explicit/explicit dynamic scheme. Computer Methods in Applied Mechanics and Engineering 2009; 198: 2318–2328.

3. Bathe KJ. Finite Element Procedures. Prentice-Hall: Englewood; 2000.

4. Belytschko T, Black T. Elastic crack growth in finite elements with minimal remeshing. International Journal for numerical methods in engineering 1999; 45(5): 601-620.

5. Moes N, Dolbow J, Belytschko T. A finite element method for crack growth without remeshing. International Journal for numerical methods in engineering 1999; 46(1): 131-150.

6. Babuška I, Melenk JM. The partition of unity method. International Journal for Numerical Methods in Engineering 1997; 40: 727-758.

7. Talebi H, Samaniego C, Samaniego E, Rabczuk T. On the numerical stability and mass-lumping schemes for explicit enriched meshfree methods. International Journal for numerical methods in engineering 2012; 89(8): 1009-1027.

8. Belytschko T, Lu YY, Gu L. Element free Galerkin methods. International Journal for Numerical Methods in Engineering 1994; 37(2):229-256.

9. Belytschko T, Tabbara M. Dynamic fracture using element-free Galerkin methods. International Journal for Numerical Methods in Engineering 1996; 39(6): 923-938.

10. Rabczuk T, Zi G. A Meshfree Method based on the Local Partition of Unity for Cohesive Cracks. Computational Mechanics 2007, 39(6): 743-760.

11. Rabczuk T, Bordas S, Zi G. A three-dimensional meshfree method for static and dynamic multiple crack nucleation/propagation with crack path continuity. Computational Mechanics 2007; 40(3):473-495.

12. Ventura G, Xu J, Belytschko T. A vector level set method and new discontinuity approximations for crack growth by EFG. International Journal for Numerical Methods in Engineering 2002; 54(6):923–944.

13. Zhuang X, Augarde C, Mathisen K. Fracture modelling using meshless methods and level sets in 3D: framework and modelling. International Journal for Numerical Methods in Engineering 2012; 92: 969-998.

14. Sukumar N, Chopp D L, Moës N, Belytschko T. Modeling holes and inclusions by level sets in the extended finite-element method. Computer methods in applied mechanics and engineering 2001; 190(46): 6183-6200.

15. Sukumar N, Moës N, Moran B, Belytschko T. Extended finite element method for three-dimensional crack modelling. International Journal for Numerical Methods in Engineering 2000; 48(11): 1549-1570.

16. Moës N, Gravouil A, Belytschko T. Non-planar 3D crack growth by the extended finite element and level sets-Part I: Mechanical model. International Journal for Numerical Methods in Engineering2002; 53(11): 2549-2568.

17. Gravouil A, Moës N, Belytschko T. Non-planar 3D crack growth by the extended finite element and level sets-Part II: Level set update. International Journal for Numerical Methods in Engineering, 2002, 53(11): 2569-2586.

18. Belytschko T, Chen H, Xu J, Zi G. Dynamic crack propagation based on loss of hyperbolicity and a new discontinuous enrichment. International journal for numerical methods in engineering 2003; 58(12): 1873-1905.

19. Hughes TJR, Liu WK. Implicit–explicit finite elements in transient analysis: implementation and numerical examples. Journal of Applied Mechanics 1978; 45:375–378.

20. de Borst R, Remmers JJC, Needleman A. Mesh-independent discrete numerical representations of cohesive-zone models. Engineering fracture mechanics 2006; 73(2): 160-177.

21. Rabczuk T, Zi G, Bordas S, Nguyen-Xuan H. A simple and robust three-dimensional cracking-particle method without enrichment. Computer Methods in Applied Mechanics and Engineering 2010; 199(37): 2437-2455.

22. Menouillard T, Rethore J, Combescure A, Bung H. Efficient explicit time stepping for the eXtended Finite Element Method (X-FEM). International Journal for Numerical Methods in Engineering, 2006, 68(9): 911-938.

23. Menouillard T, Rethore J, Moes N, Combescure M, Bung H. Mass lumping strategies for X-FEM explicit dynamics: application to crack propagation. International Journal for Numerical Methods in Engineering 2008; 74(3):447-474.

24. Schweitzer MA. Variational mass lumping in the partition of unity method. SIAM Journal on Scientific Computing 2013; 35(2): A1073-A1097.

25. Piedade Neto D, Baroncini Proenca SP. Generalized Finite Element Method in linear and nonlinear structural dynamic analyses. Engineering Computations 2016; 33(3): 806-830.

26. Shi GH. Manifold method of material analysis. In: Proceedings of the transactions of the Ninth Army Conference on Applied Mathematics and Computing; 1991: 57-76.

27. Shi GH. Discontinuous deformation analysis - a new numerical model for the statics and dynamics of block systems. Ph.D. Thesis, University of California, Berkeley, 1988.

28. Zheng H, Zhang P, Du XL. Dual form of discontinuous deformation analysis. Computer Methods in Applied Mechanics and Engineering 2016; 305: 196-216.

29. Zhang HH, Li LX, An XM, Ma GW. Numerical analysis of 2-D crack propagation problems using the numerical manifold method. Engineering Analysis with Boundary Elements 2010; 34: 41-50.

30. Tsay RJ, Chiou YJ, Chuang WL. Crack growth prediction by manifold method. Journal of Engineering Mechechanics – ASCE 1999; 125(8): 884-890.

31. Liu ZJ, Zheng H. Two-dimensional numerical manifold method with multilayer covers. Science China – Technological Sciences 2015; online, doi:10.1007/ s11431-015-5907-z.

32. Zheng H, Liu F, Du XL. Complementarity problem arising from static growth of multiple cracks and MLS-based numerical manifold method. Computer Methods in Applied Mechanics and Engineering 2015; 295: 150-171.

33. Ma GW, An XM, Zhang HH, Li LX. Modelling complex crack problems using the numerical manifold method. International Journal of Fracture 2009; 156: 21-35.

34. Wu ZJ, Wong LNY, Fan LF. Dynamic study on fracture problems in viscoelastic sedimentary rocks using the numerical manifold method. Rock mechanics and rock engineering 2013; 46(6): 1415-1427.

35. Zheng H, Liu ZJ, Ge XR. Numerical manifold space of Hermitian form and application to Kirchhoff's thin plate problems. International Journal for Numerical Methods in Engineering 2013; 95: 721–739.

36. Jiang QH, Deng SS, Zhou CB, Lu WB. Modeling unconfined seepage flow using three-dimensional numerical manifold method. Journal of Hydrodynamics 2010; 22: 554-561.

37. Wang Y, Hu MS, Zhou QL, Rutqvist J. Energy-work-based numerical manifold seepage analysis with an efficient scheme to locate the phreatic surface, International Journal for Numerical and Analytical Methods in Geomechanics 2014; 38: 1633-1650.

38. Zheng H, Liu F, Li CG. Primal mixed solution to unconfined seepage flow in porous media with numerical manifold method. Applied Mathematical Modelling 2015; 39: 794-808.

39. Qu XL, Fu GY, Ma GW. An explicit time integration scheme of numerical manifold method. Engineering Analysis with Boundary Elements 2014; 48: 53-62.

40. Qu XL, Wang Y, Fu GY, Ma GW. Efficiency and accuracy verification of the explicit numerical manifold method for dynamic problems. Rock Mechanics and Rock Engineering 2015; 48(3): 1131-1142.

41. Zheng H, Xu DD. New strategies for some issues of numerical manifold method in simulation of crack propagation. International Journal for Numerical Methods in Engineering 2014; 97(13): 986-1010.

42. Song JH, Areias PMA, Belytschko T. A method for dynamic crack and shear band propagation with phantom nodes. International Journal for Numerical Methods in Engineering 2006; 67: 868–893.

43. Zheng H, Liu F, Li CG. The MLS-based numerical manifold method with applications to crack analysis. International Journal of Fracture 2014; 190: 47–166.

44. Munkres JR. Analysis on manifolds. Addison-Wesley Publishing Company, Redwood City, 1991.

45. Liu GR. On Partitions of Unity Property of Nodal Shape Functions: Rigid-Body-Movement Reproduction and Mass Conservation. International Journal of Computational Methods 2016; 13(2), 1640003.

46. He ZC, Li E, Liu GR, Li GY, Cheng AG. A mass-redistributed finite element method (MR-FEM) for acoustic problems using triangular mesh. Journal of Computational Physics 2016; 323: 149-170.

47. He ZC, Li G, Zhang G, Liu GR, Gu Y, Li E. Acoustic analysis using a mass-redistributed smoothed finite element method with quadrilateral mesh. Engineering Computations 2015; 32 (8), 2292-2317.

48. Freund LB. Dynamic fracture mechanics. Cambridge University Press, London, 1998.

49. Liu P, Bui TQ, Zhang Ch, Yu TT, Liu GR, Golub MV. The singular edge-based smoothed finite element method for stationary dynamic crack problems in 2D elastic solids. Computer Methods in Applied Mechanics and Engineering 2012; 233: 68-80.

50. Belytschko T, Guo Y, Liu WK, Xiao SP. A unified stability analysis of meshfree particle methods. International Journal for Numerical Methods in Engineering 2000; 48:1359–1400.

51. Menouillard T, Belytschko T. Dynamic fracture with meshfree enriched XFEM. Acta Mechanica, 2010, 213(1-2): 53-69.

52. Belytschko T, Chen H. Singular enrichment finite element method for elastodynamic crack propagation. International Journal of Computational Methods 2004; 1(01): 1-15.

53. Candy J, Rozmus W. A symplectic integration algorithm for separable Hamiltonian functions. Journal of Computational Physics archive 1991; 92(1): 230 – 256.

Table 1 Critical time steps without discontinuity

Critical time step	Mesh 5×5	Mesh 10×10
$\Delta t_{consist}$	1.3×10^{-4}	6.4×10^{-5}
Δt_{lump}	2.3×10^{-4}	1.2×10^{-4}
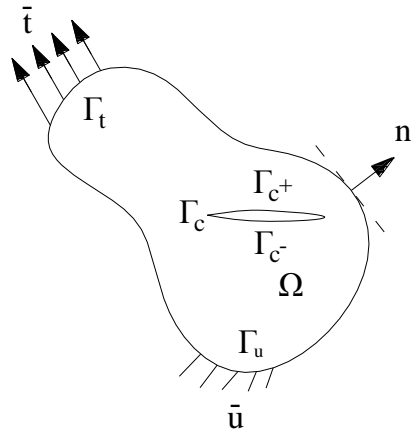
Figure 1 A 2-D elastic cracked body.
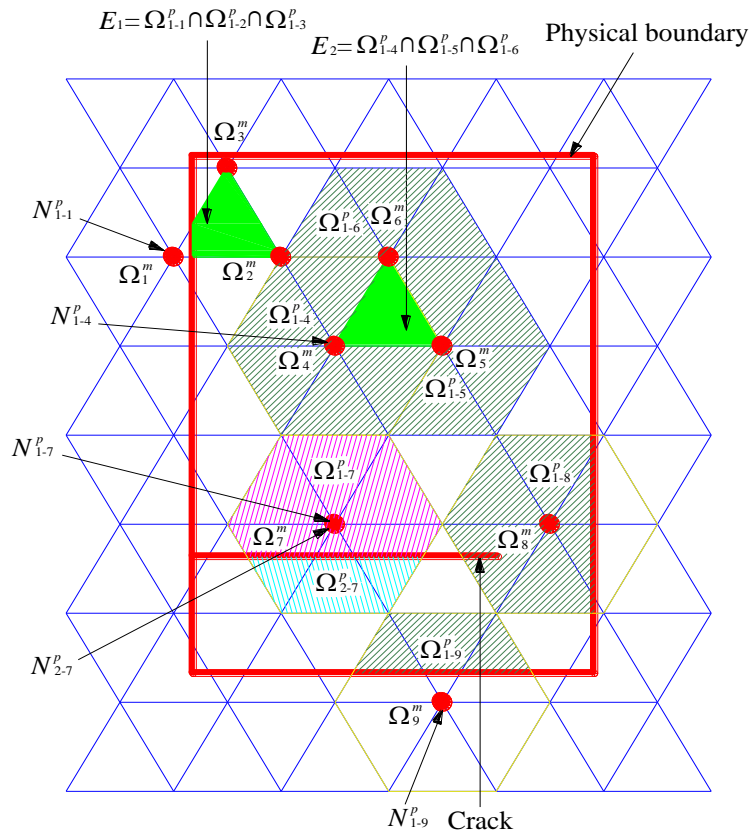
Figure 2 Mathematical patches, physical patches and manifold elements in NMM.
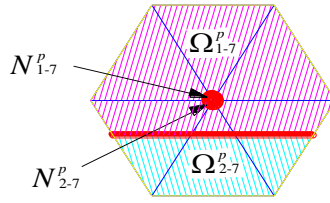
(a) At the outset, real node $N_{1\text{-}7}^{p}$ and phantom node $N_{2\text{-}7}^{p}$ coincide
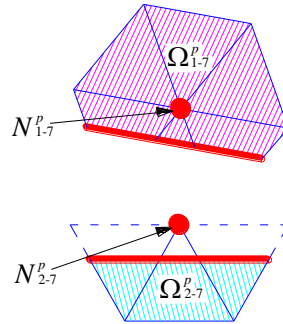
(b) If large movement occurs, real node $N_{1\text{-}7}^{p}$ and phantom node $N_{2\text{-}7}^{p}$ separate

Figure 3 Interpretation of real and phantom nodes.
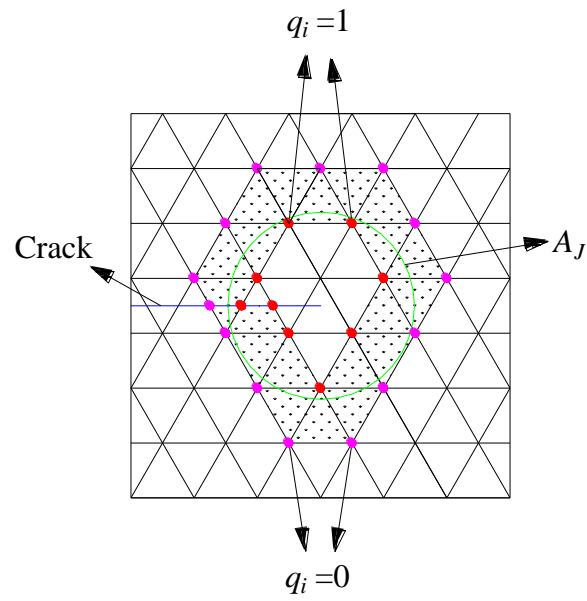
Figure 4 Area path of interaction integral A_J and definition of q.

(a) no crack is considered

(b) crack varies vertically in [4, 6]

(c) crack varies vertically in [4, 6]

(d) crack tip varies horizontally in [4, 6]
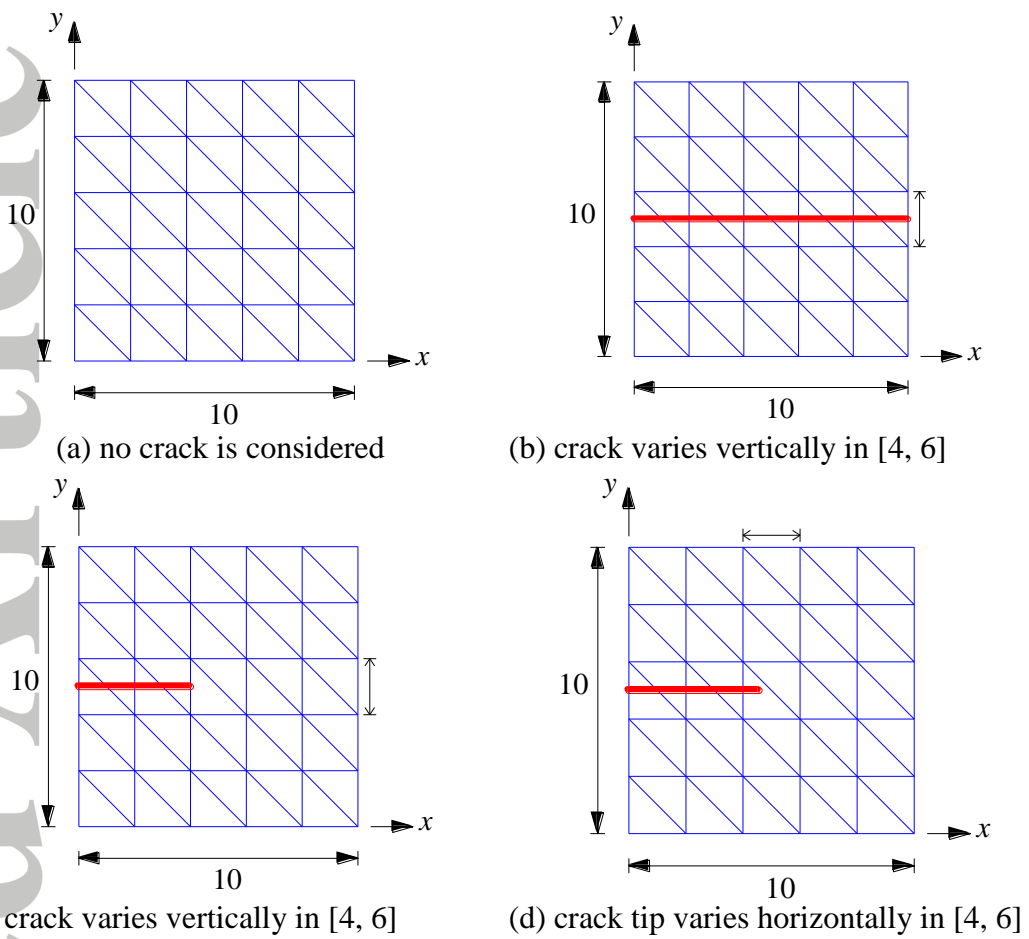
Figure 5 Mesh 5×5 to compute critical time step of different crack position

(a) no crack is considered

(b) crack varies vertically in [5, 6]

(c) crack varies vertically in [5, 6]

(d) crack tip varies horizontally in [5, 6]
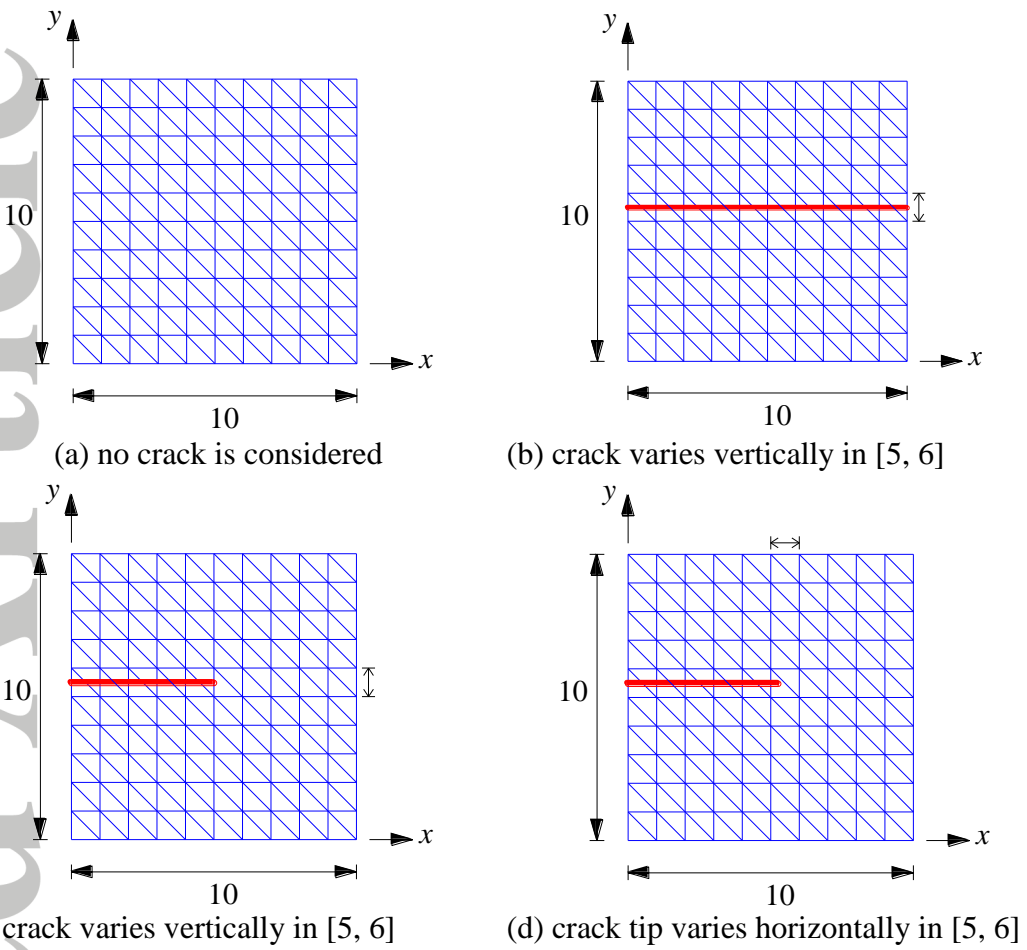
Figure 6 Mesh 10×10 to compute critical time step of different crack position

(a) crack cut through domain (Fig. 5(b))

(b) crack varies vertically (Fig. 5(c))

(c) crack varies horizontally (Fig. 5(d))
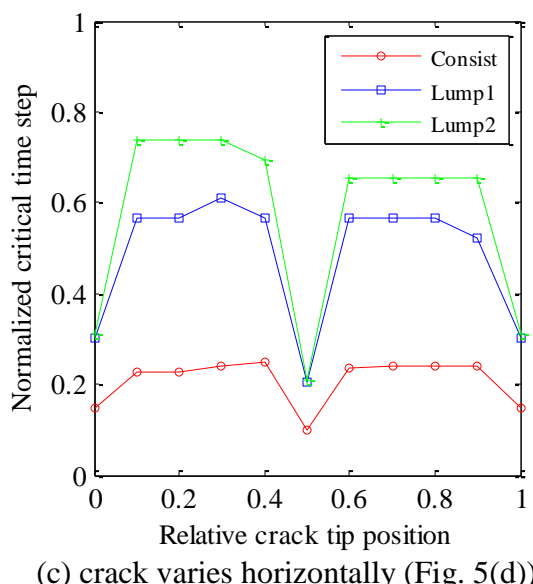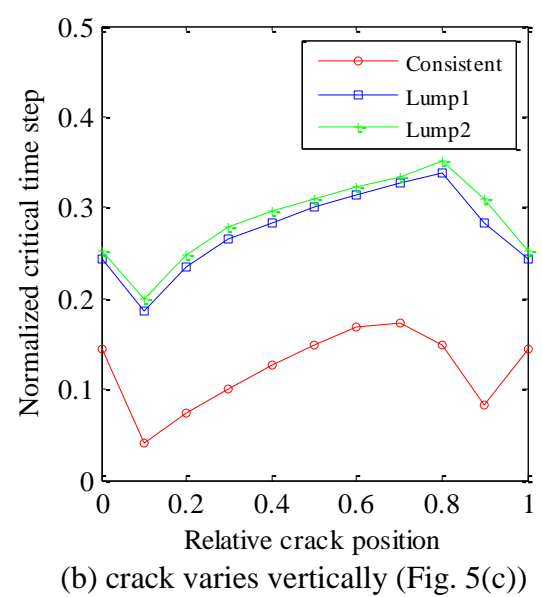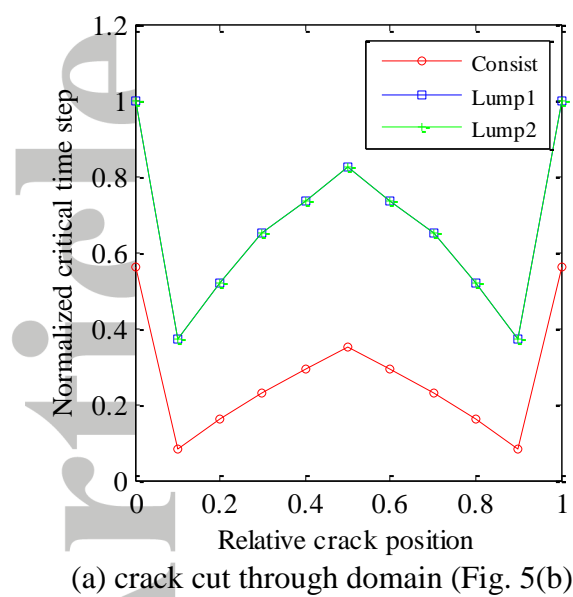
Figure 7 Critical time step of mesh 5×5 *vs* crack position for $\boldsymbol{M}_{consist}$ and $\boldsymbol{M}_{lump}$

(a) crack cut through domain (Fig. 6(b))

(b) crack varies vertically (see Fig. 6(c))

(c) crack varies horizontally (Fig. 6(d))
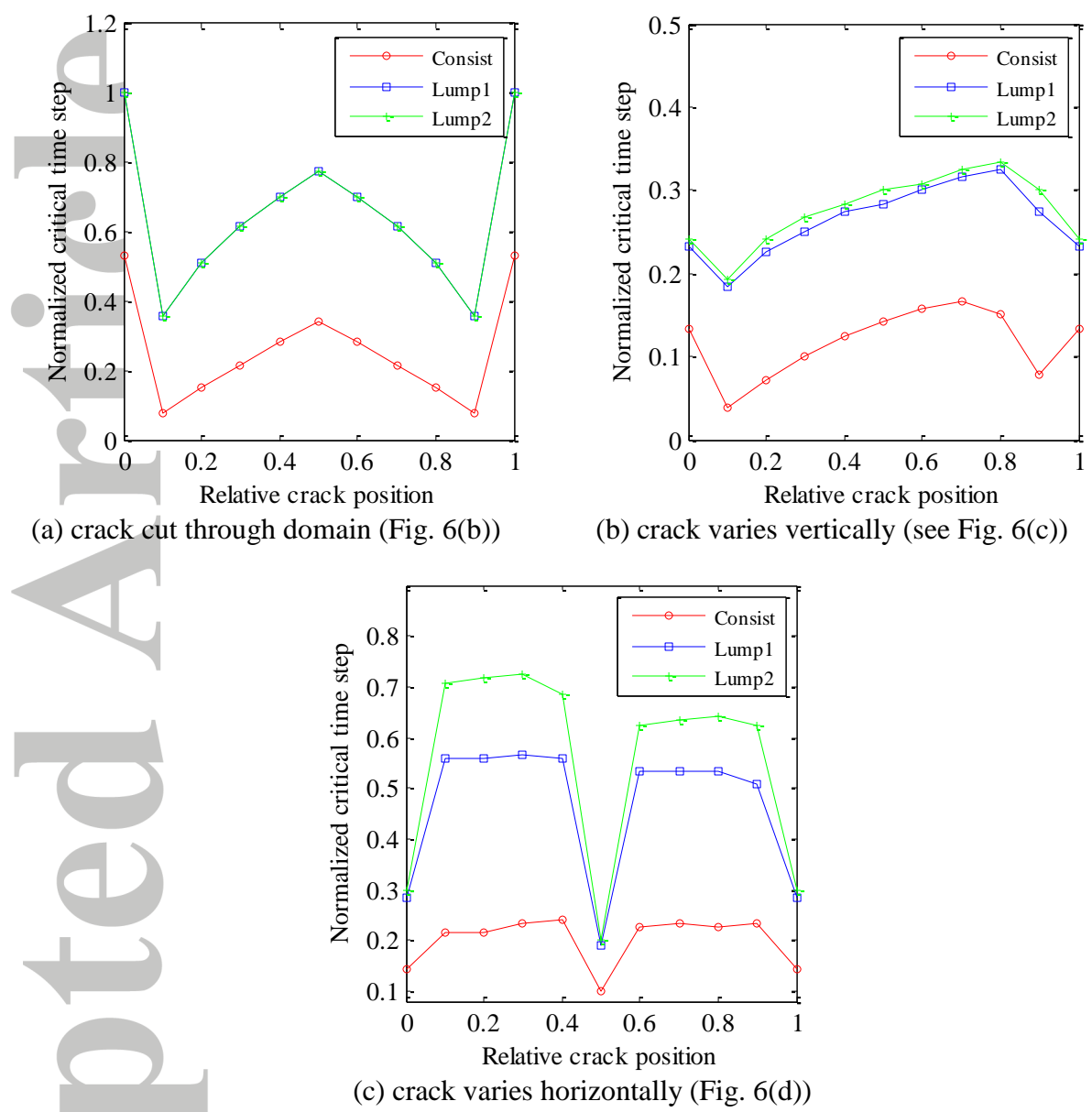
Figure 8 Critical time step of mesh 10×10 *vs* crack position $M_{consist}$ and M_{lump}
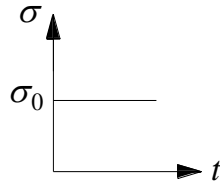
Figure 9 Heaviside step load.
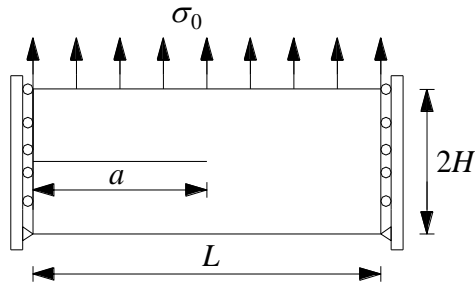
Figure 10 Finite geometry of semi-infinite crack problem.
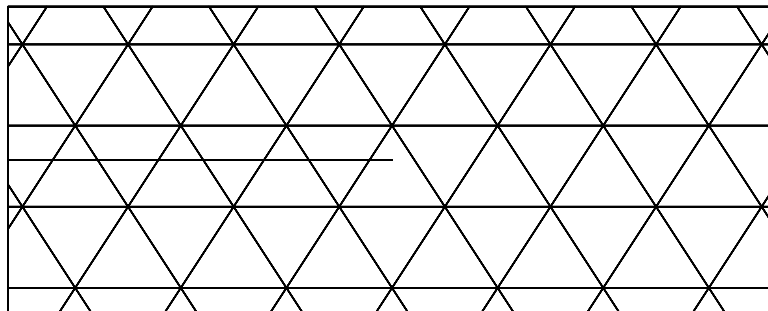
(a) 62 PPs
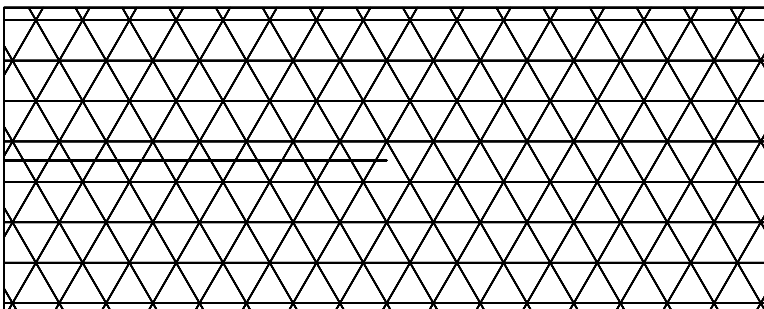
(b) 199 PPs
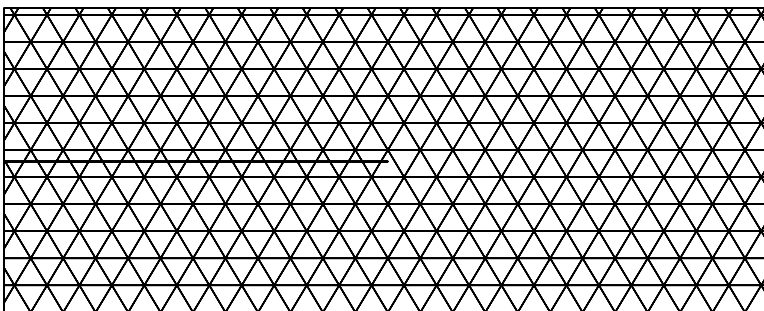
(c) 378 PPs

Figure 11 Discretized models of a semi-infinite crack.
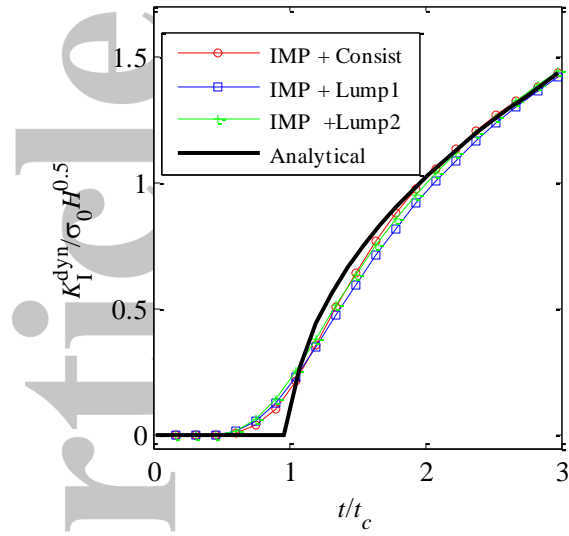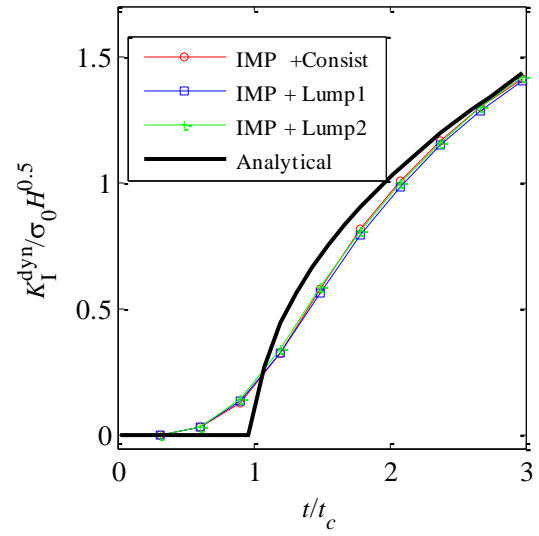
(a) $\Delta t = 50$ μs   (b) $\Delta t = 100$ μs

Figure 12 Comparison of accuracy of different mass matrices using implicit time integration (378 PPs). IMP = implicit time integration plus NMM. Consist = consistent mass matrix. Lump1 and Lump2 indicate M_{lump} corresponding to equation (39) and equation (41), respectively.
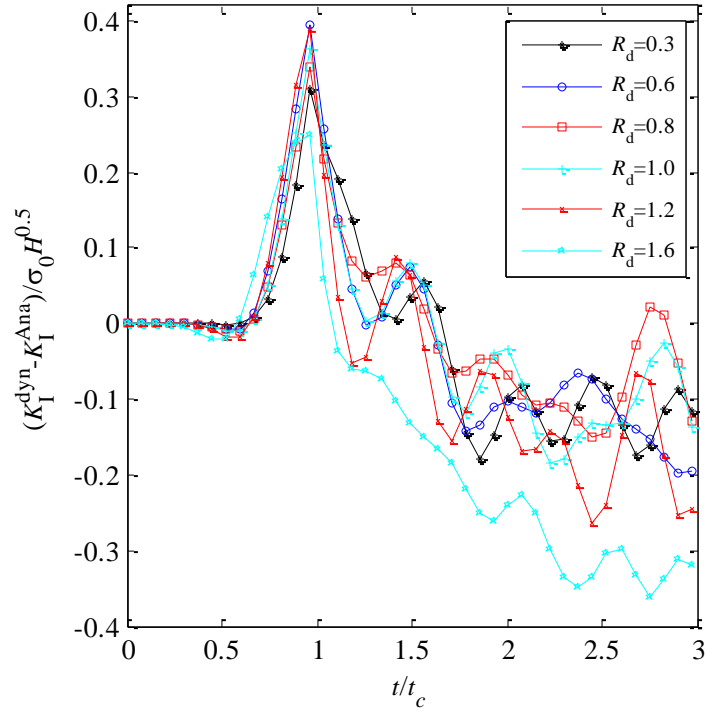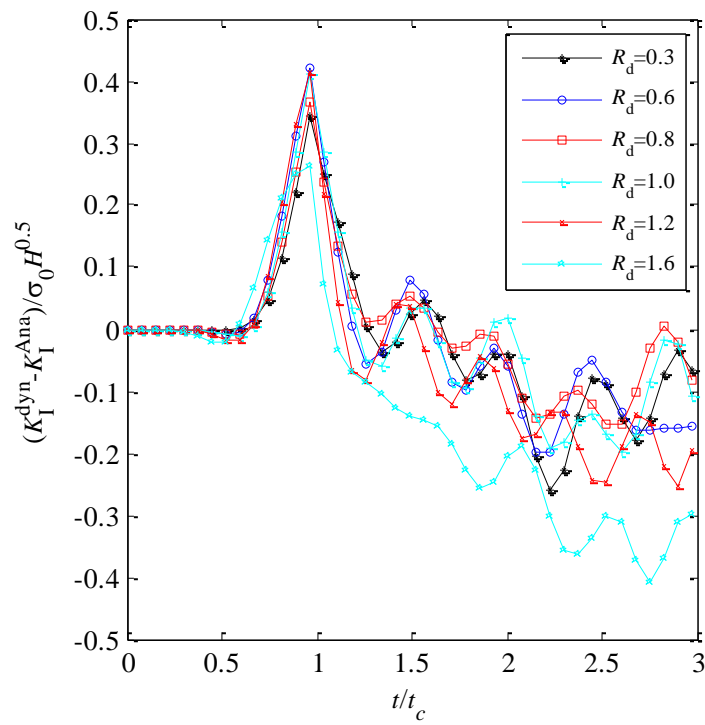
(a) EXP + Lump1

(b) EXP + Lump2

Figure 13. The effect of integration domain size on DSIF
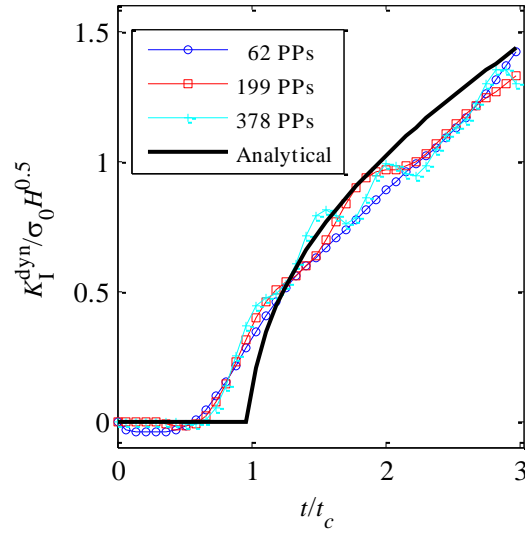
(a) EXP + Lump1
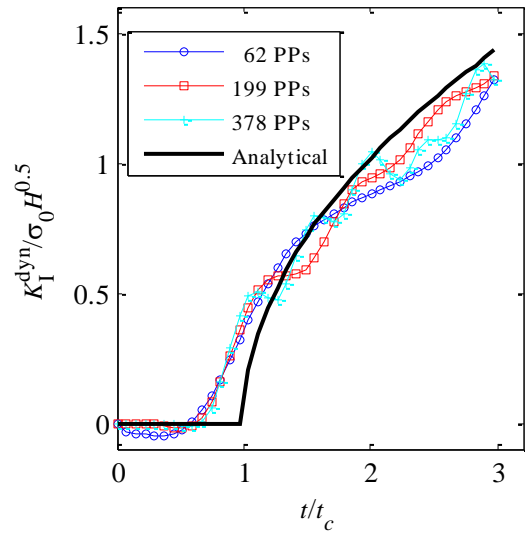
(b) EXP + Lump2

Figure 14 Convergence of DSIF for semi-infinite crack
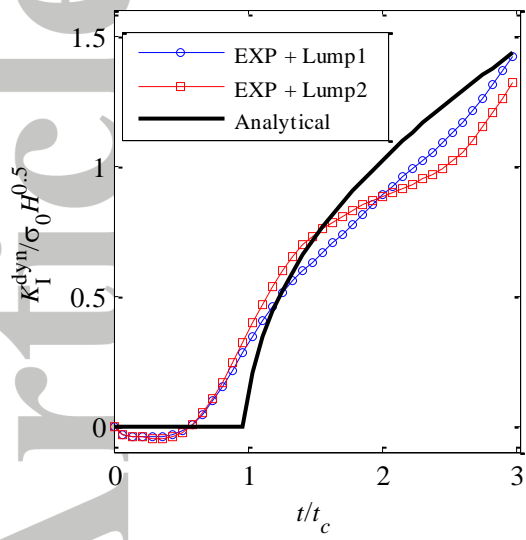
(a) 62 PPs
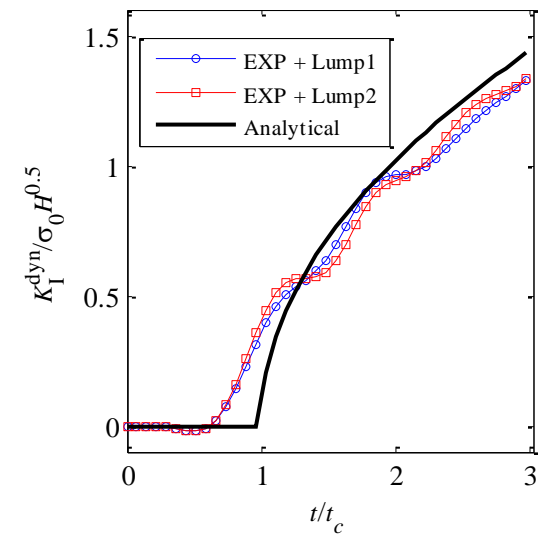
(b) 199 PPs
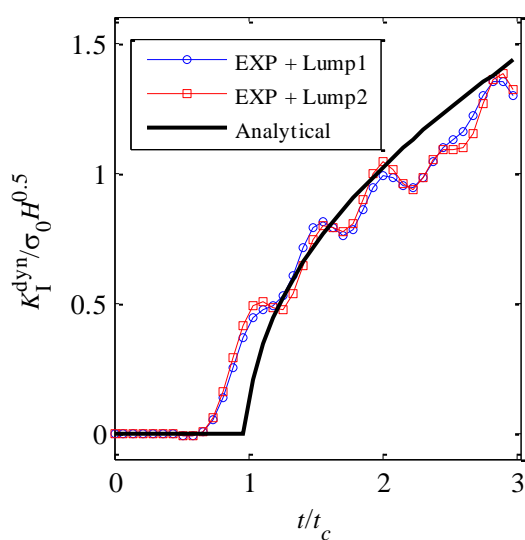
(c) 378 PPs

Figure 15 Comparison of accuracy by EXP + Lump1 and EXP + Lump2 with different mesh density
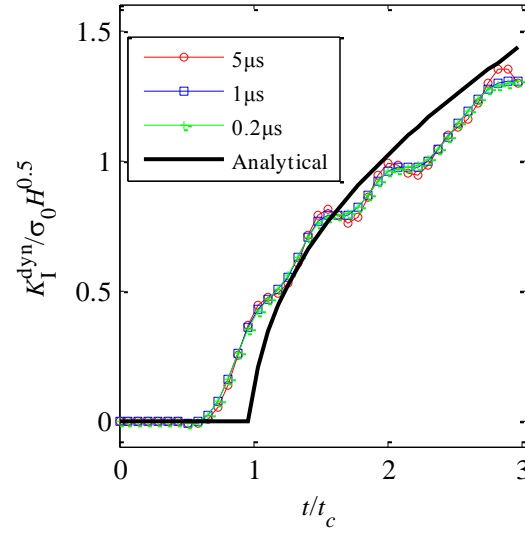
(a) EXP + Lump1
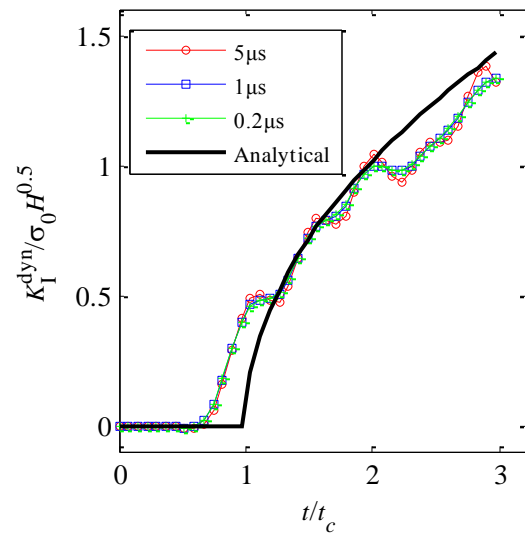
(b) EXP + Lump2

Figure 16 The effect of time step on DSIF.

(a) 5 μs

(b) 1 μs

(c) 0.2 μs
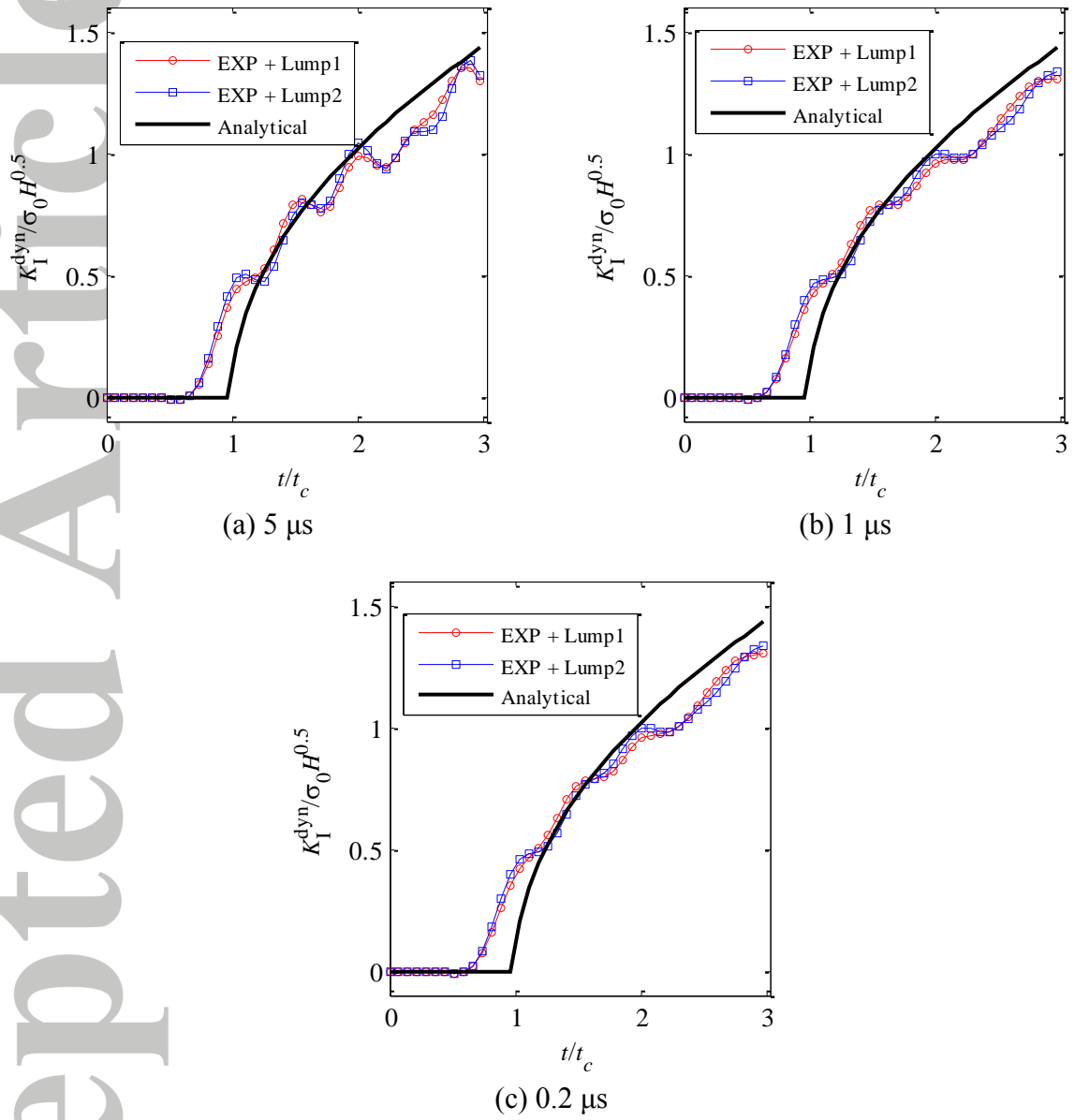
Figure 17 Comparison of accuracy of EXP + Lump1 and EXP + Lump2 with different time step.
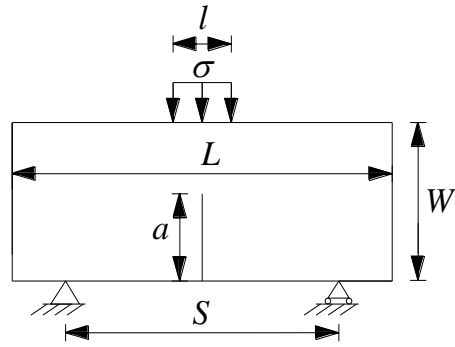
Figure 18 Geometry of a three-point-bending beam
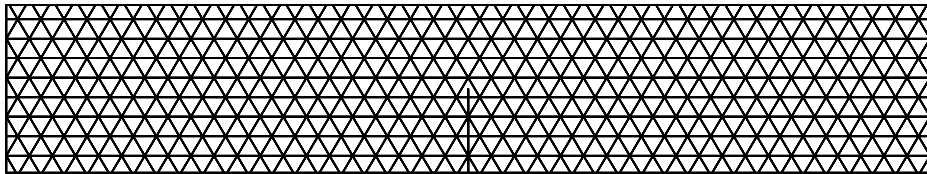
Figure 19 Discretized model of a three-point-bending beam (421 PPs).
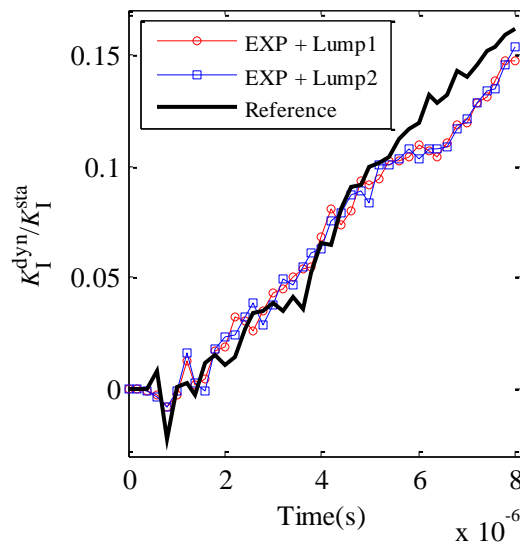
Figure 20 Comparison of accuracy by EXP + Lump1 and EXP + Lump2 on DSIF for the three point bending beam.
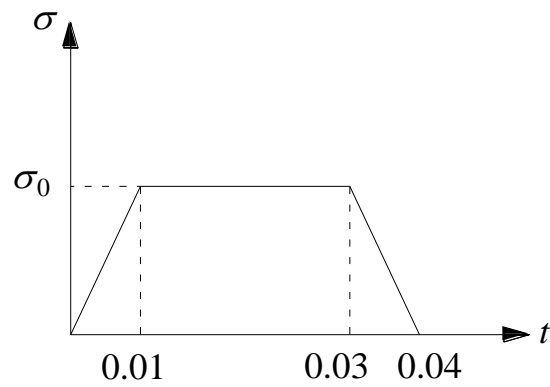
Figure 21 Tension-time curve acting on upper beam in laminated cantilever in Fig. 22
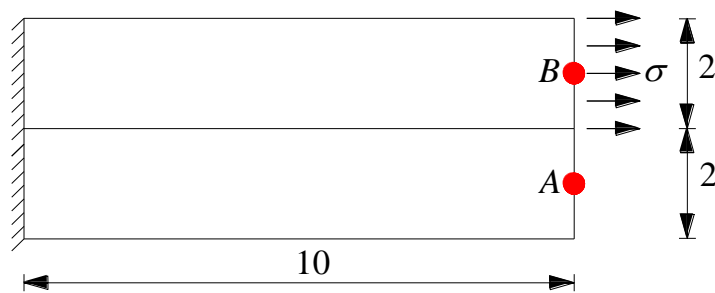
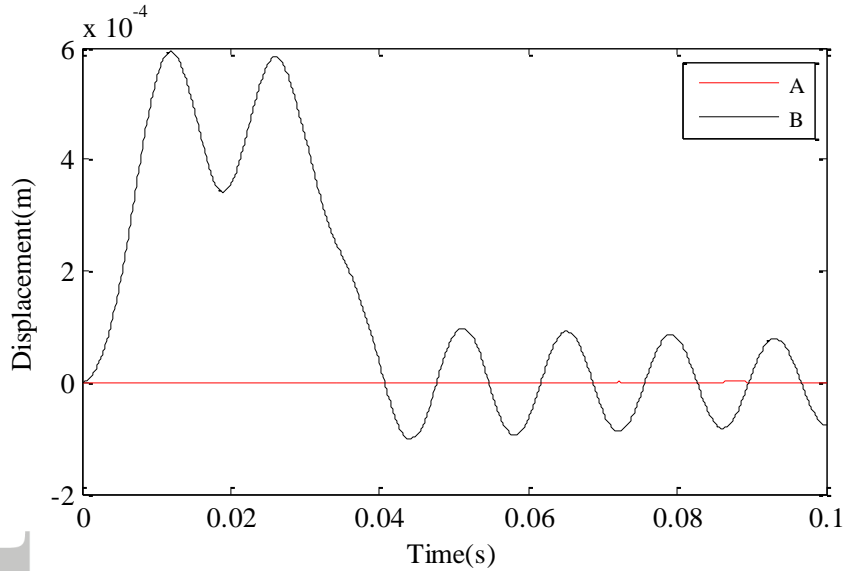Figure 22 Geometry of a sample with a cutting through crack.
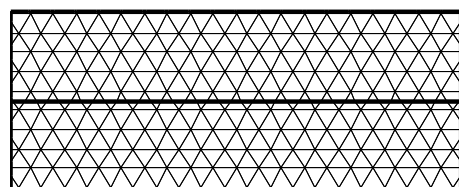
Figure 23 Discretized model of a cantilever (299 patches)
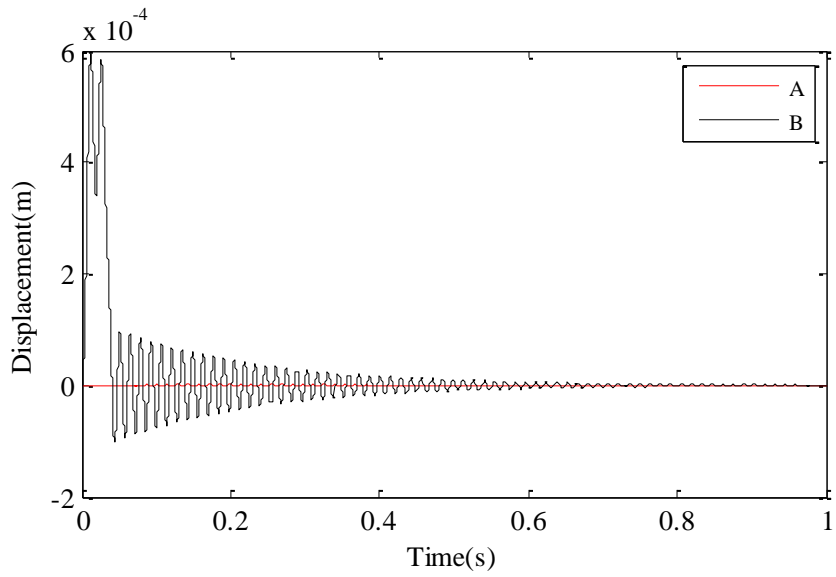
(a) u_x – time curves during 0 to 1 s

(b) Details of u_x in [0, 0.1]

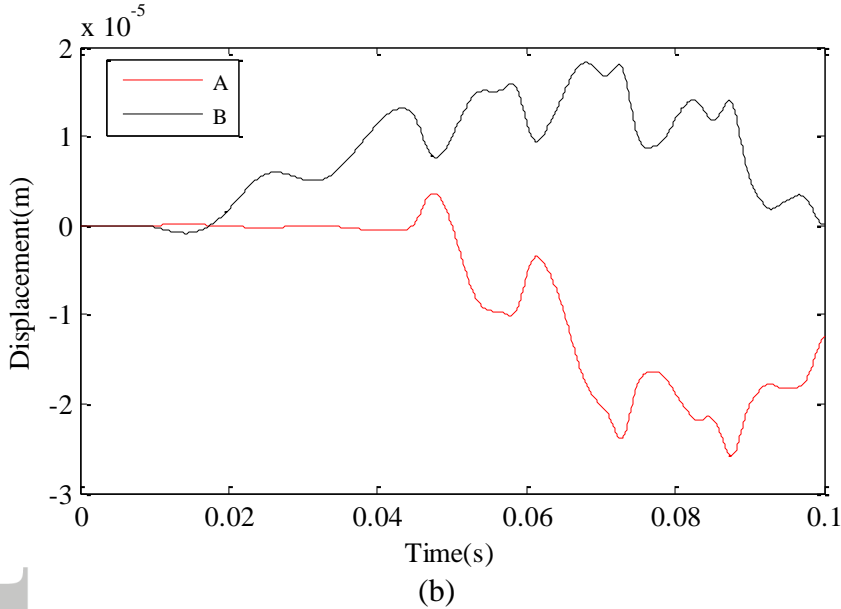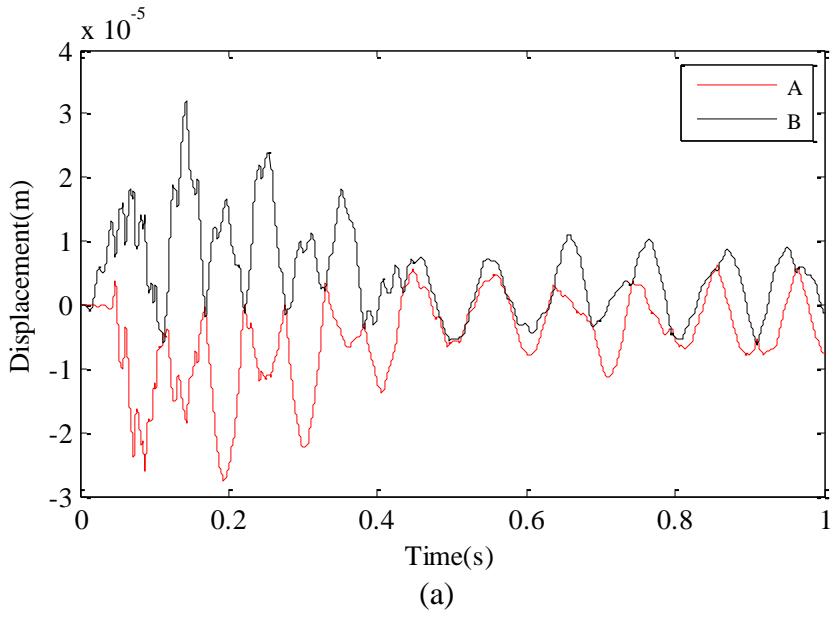Figure 24 Horizontal displacement u_x of monitored points A and B.

(a)

(b)

Figure 25 Vertical displacement of monitored points A and B